



# Rising vegetation activity dominates growing water use efficiency in the Asian permafrost region from 1900 to 2100

Fenghui Yuan<sup>a,b,c</sup>, Jianzhao Liu<sup>a</sup>, Yunjiang Zuo<sup>a,e</sup>, Ziyu Guo<sup>a</sup>, Nannan Wang<sup>c,d,e</sup>, Changchun Song<sup>a</sup>, Zongming Wang<sup>a</sup>, Li Sun<sup>a</sup>, Yuedong Guo<sup>a</sup>, Yanyu Song<sup>a</sup>, Dehua Mao<sup>a</sup>, Feifan Xu<sup>a</sup>, Xiaofeng Xu<sup>c,\*</sup>

<sup>a</sup> Key Laboratory of Wetland Ecology and Environment, Northeast Institute of Geography and Agroecology, Chinese Academy of Sciences, Changchun 130102, China

<sup>b</sup> Key Laboratory of Forest Ecology and Management, Institute of Applied Ecology, Chinese Academy of Sciences, Shenyang 110016, China

<sup>c</sup> Biology Department, San Diego State University, San Diego, CA 92182, USA

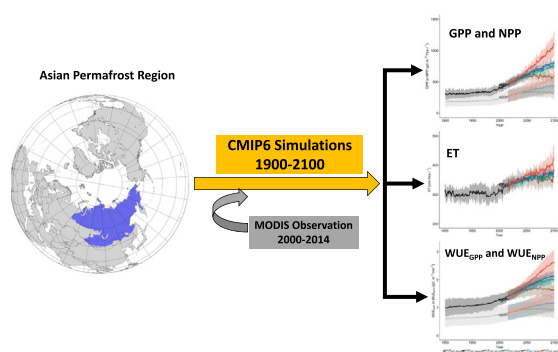
<sup>d</sup> State Key Laboratory of Vegetation and Environmental Change, Institute of Botany, Chinese Academy of Sciences, Beijing 100093, China

<sup>e</sup> University of Chinese Academy of Sciences, Beijing 100080, China

## HIGHLIGHTS

- Rising vegetation activity dominates the climbing water use efficiency in the Asian permafrost region from 1900 to 2100.
- Large spatial heterogeneities in water and carbon fluxes were observed in the study domain.
- The CMIP6 models projected substantial increases in GPP and NPP while slight increase in evapotranspiration during 2010–2100.

## GRAPHICAL ABSTRACT



## ARTICLE INFO

### Article history:

Received 10 April 2020

Received in revised form 19 May 2020

Accepted 19 May 2020

Available online 21 May 2020

Editor: Fernando A.L. Pacheco

### Keywords:

Climate change

CMIP6

Earth system model

Siberia

WUE

### Data availability:

All CMIP6 model outputs can be obtained from the Lawrence Livermore National Laboratory

## ABSTRACT

Permafrost play an important role in regulating global climate system. We analyzed the gross primary productivity (GPP), net primary productivity (NPP), and evapotranspiration (ET) derived from MODIS and three earth system models participated in the Coupled Model Inter-comparison Project Phase 6 (CMIP6) in the Asian permafrost region. The water use efficiency (WUE) was further computed. The simulated GPP, NPP, and ET show slightly increasing trends during historical period (1900–2014) and strong increasing trends in projection period (2015–2100), and projected impacts of climate change on all variables are greater under high-emission scenarios than low-emission scenarios. Further analysis revealed higher increases in GPP and NPP than that of ET, indicating that vegetation carbon sequestration governs the growing WUE under historical and projected periods in this region. The GPP, NPP and ET showed higher changing rates in western, central and southeast areas of this region, and WUE (WUE<sub>GPP</sub>, and WUE<sub>NPP</sub>) shows the similar spatial pattern. Compared to MODIS-derived GPP, NPP, and ET during 2000–2014, Earth system models yield the best estimates for NPP, while slight underestimations for GPP and ET, and thus slight overestimations for WUE<sub>GPP</sub> and WUE<sub>NPP</sub>. This study highlights the predominant role of vegetation activity in regulating regional WUE in Asian permafrost region under future climate change. Vegetation domination of the growing water use efficiency implies that the permafrost region may continue acting efficiently in sequestering atmospheric carbon in terms of water consumption throughout the 21st century.

\* Corresponding author.

E-mail address: [xxu@sdsu.edu](mailto:xxu@sdsu.edu) (X. Xu).

(LLNL) node (<https://esgf-node.llnl.gov/projects/cmip6>). MODIS datasets are available from the Numerical Terradynamic Simulation Group (NTSG) of University of Montana ([www.ntsg.umt.edu/project/modis](http://www.ntsg.umt.edu/project/modis)).

© 2020 The Authors. Published by Elsevier B.V. This is an open access article under the CC BY-NC-ND license (<http://creativecommons.org/licenses/by-nc-nd/4.0/>).

## 1. Introduction

Permafrost, a globally significant carbon pool, has been found to be vulnerable and sensitive to the recent changes in global climate system, owing to its unique physical and biological characteristics (McGuire et al., 2009). Over the past few decades, investigation into the permafrost carbon dynamics has made significant progress. Studies found that vegetation activities (Jin et al., 2017; White et al., 1999) and growing season length (Zhu et al., 2016) can be altered by climate change along with thawing permafrost (Schuur et al., 2008). Climate change directly or indirectly alter surface energy balance and soil hydraulic and thermal properties and moisture regimes in the permafrost region (Bring et al., 2016; Hinzman et al., 2005), which further strongly affect the vegetation carbon sequestration (Jung et al., 2010). Although substantial progress has been made, there are large uncertainties in the understanding of the carbon cycling in permafrost region. For example, the instability of carbon sink could occur as a result of a climate-caused vegetation shift between boreal forests and tundra (Euskirchen et al., 2009). Hence, understanding the carbon dynamics in response to climate change is crucial to our predictability of the permafrost-climate feedback.

Gross primary production (GPP) and net primary production (NPP) represent the primary inputs of carbon to the terrestrial systems, and evapotranspiration (ET) is a major component of the water cycle, as the sum of soil evaporation, vegetation transpiration, and canopy evaporation of intercepted precipitation. Furthermore, water use efficiency (WUE), defined as vegetation carbon sequestration per unit of water loss, has been frequently utilized as an important indicator quantifying the coupling between water and carbon cycles (Cheng et al., 2017; Song et al., 2013; Tian et al., 2010). It is crucial to understand how permafrost responds to the projected climate change, by identifying long-term pattern and the dominant factors of WUE. The positive impacts of climate warming and elevated CO<sub>2</sub> on carbon sequestration (Xia et al., 2017) and ET (Brutsaert, 2006; Yan et al., 2013; Zeng et al., 2012; Zhang et al., 2015) have been widely reported in the northern permafrost regions. The neutral impact of elevated CO<sub>2</sub> on vegetation carbon sequestration is also reported in permafrost regions (Körner et al., 1997; Oberbauer et al., 1986). For the ET in the permafrost regions, studies found declining trends (Peterson et al., 1995; Jung et al., 2010), or no trend (Badgley et al., 2015; Zhang et al., 2016) due to soil moisture limitation (Jung et al., 2010) and shifting vegetation physiology (Badgley et al., 2015; Cheng et al., 2017; Zhang et al., 2016). In summary, vegetation carbon sequestration and evapotranspiration in the permafrost regions have been intensively studied, yet how do WUE respond to climate change in the permafrost regions remain unclear.

The permafrost area in Asia accounts for more than half of the Northern Hemisphere's total permafrost area. No general conclusions on the carbon and water cycling in the northern hemisphere permafrost area have been drawn, as it is challenging to have a comprehensive understanding of carbon and water cycling in this region (Romanovsky et al., 2010). Asian permafrost region has long been studied (Shiklomanov, 2005). For example, studies have mentioned the historical and projected trends of carbon gain or ET by the classification of tundra and boreal forest biomes in nearby area or part of the region (Chen et al., 2017; Jung et al., 2010; Propastin and Kappas, 2012; Zeng et al., 2012; Zhang et al., 2014b), based on integrated observation and satellite data or model simulations. However, none of them has focused

on the long-term spatiotemporal patterns of carbon sequestration and water flux.

Recently, Shared Socioeconomic Pathways (SSPs) have been released for climate change research and assessment with the Coupled Model Intercomparison Project Phase 6 (CMIP6) experiments (Eyring et al., 2016). The SSPs represent state-of-the-art prototypical pathways for global environmental change during the 21st century, with SSP1 Sustainability, SSP2 Middle of the road, SSP3 Regional rivalry, SSP4 Inequality, and SSP5 Fossil fueled development (Eyring et al., 2016). Different emission scenarios are considered to better represent the future climate projections (Eyring et al., 2016). The new scenarios in CMIP6 are based on a matrix that uses the SSPs and forcing levels of the Representative Concentration Pathways (RCP) as axes (Eyring et al., 2016). Several SSP scenarios for which the equivalent concentration pathway as CMIP5 RCPs are available within the CMIP6 simulations. As such, SSP126, SSP245, SSP460 and SSP585 were consistent with RCP2.6, RCP4.5, RCP6.0, and RCP8.5, respectively (O'Neill et al., 2016).

In this study, we used the simulated CMIP6 outputs of vegetation carbon gain (GPP and NPP), water loss (ET), and WUE (WUE<sub>GPP</sub> and WUE<sub>NPP</sub>) to investigate their trends over the Asian permafrost region during the period of 1900 to 2100. Specifically, we focus on three key questions: (1) how do vegetation carbon gain, water loss and WUE change over 1900–2100? (2) What are the different responses of all variables among different climate scenarios? (3) What are the dominating variables contributing to the changing WUE? The outputs of earth system models participated in CMIP6 were validated by comparing against the MODIS-derived GPP, NPP and ET during 2000–2014 before the long-term analyses.

## 2. Materials and methods

### 2.1. Study area

The study area embraces continuous permafrost region in the Asian continent (45°N ~ 85°N, 60°E ~ 170°W; Fig. 1). The data set was derived from the circumpolar permafrost and ground ice data of the National Snow and Ice Data Center (Brown et al., 2002). The area spans large areas of Russia, Mongolia, and some parts of China and Kazakhstan, totally covering 12 million km<sup>2</sup>, approximately 53% of the total permafrost area in northern hemisphere.

Global atmospheric reanalysis II data of the National Centers for Environmental Prediction (NCEP-2) showed a mean annual air temperature of −5.55 °C and mean annual precipitation of 575.7 mm between 2000 and 2014 in this area. Over the same period, average minimum air temperature was as low as −44.87 °C, and average maximum temperature was 26.40 °C. This area has long cold winters and short summers.

According to the Moderate Resolution Imaging Spectroradiometer (MODIS) land cover data from 2010 (Friedl et al., 2010), which is based on the classification scheme proposed by the International Geosphere-Biosphere Programme (IGBP), the predominant land cover type in this area is open shrublands (53.2%), followed by mixed forest (12.4%), deciduous needleleaf forest (10.4%), grassland (9.4%), woody savannas (5.97%) and permanent wetlands (2.4%), etc. Open shrublands mostly distribute in the northern part, forests in the central, and grassland and steppe are mainly in the southern part of the study region. Based on the reanalysis of the version 1.2 of Harmonized World Soil Data (HSWD) (Wieder et al., 2014), the average soil texture of the surface soil is 51.4% sand, 31.3% silt and 14.3% clay. The bulk density is



**Fig. 1.** Location map of the study area (blue-filled). This especially area is covered with continuous permafrost, whose distribution was derived from the circumpolar permafrost and ground ice data of the National Snow and Ice Data Center (Brown et al., 2002).

approximately  $1.28 \text{ g.cm}^{-3}$  and the soil organic carbon is  $7.77 \text{ kg C.m}^{-2}$ , soil pH is about 5.65, and gravel content is 7.8%.

## 2.2. Data source

### 2.2.1. ESM outputs

Three Earth System Models (ESMs) participating in the sixth phase of the CMIP were used to analyze spatiotemporal patterns of GPP, NPP, ET and WUE during 1900–2100. The three ESMs are CNRM-ESM2–1 (Séférian, 2018), CanESM5 (Swart et al., 2019) and IPSL-CM6A-LR (Boucher et al., 2018). They were chosen because only these models produced GPP, NPP and ET variables under all four special climate scenarios (Table S1). Specifically, the land in CNRM-ESM2–1 is represented by the Soil-Biosphere-Atmosphere (ISBA) scheme; the land component of CanESM5 consists of the Canadian Land Surface Scheme (CLASS) and the Canadian Terrestrial Ecosystem Model (CTEM); IPSL-CM6A-LR is based on the Organising Carbon and Hydrology In Dynamic Ecosystems (ORCHIDEE) land model. All models participating in CMIP6 used the same standard input forcing dataset for each experiment. Further descriptions of these models and run configurations are available on the ES-DOC (<https://es-doc.org/cmip6/>) and PCMDI (<https://pcmdi.llnl.gov/CMIP6/Guide/modelers.html>) interfaces.

Given that some models had simulations with different initial conditions hereby generating single-model multi-member ensembles for the historical and future simulations, we only processed the results from the first ensemble (r1i1p1f1, r for realization, i for initialization, p for physics, and f for forcing) for each model to avoid biases among ESMs (Table S1). The historical simulation covers 1900–2014 and the future simulations cover 2015–2100. These monthly output variables were downloaded via ESGF portals at LLNL node (<https://esgf-node.llnl.gov/search/cmip6>) and then resampled to  $0.25^\circ \times 0.25^\circ$  using the first-order conservative remapping scheme.

### 2.2.2. Satellite-derived data

A long-term time series (2000–2014) of GPP, and ET data from 30-arc-sec spatial resolution MODIS products were used as the observation data to validate the model simulation results. The annual GPP and NPP products MOD17A3 were calculated by summing all 46 8-day GPP values from MOD17A2 NPP (Running et al., 2004; Zhao et al., 2005), which was developed based on a light-use efficiency model (Heinsch et al., 2003). The ET product MOD16A3 was calculated by using the improved ET algorithm based on the Penman-Monteith equation (Mu et al., 2011). All MODIS datasets were obtained from the Numerical Terrdynamic Simulation Group (NTSG) at University of Montana ([www.ntsug.umt.edu/project/modis](http://www.ntsug.umt.edu/project/modis)) and then resampled to a spatial resolution of  $0.25^\circ \times 0.25^\circ$  for comparison purpose.

## 2.3. Data analysis

In this study, two definitions of WUE for both CMIP6 and MODIS data were used to quantify the carbon uptake per unit of water lost: (1) GPP-based water use efficiency ( $\text{WUE}_{\text{GPP}}$ ) is the ratio of GPP to ET; (2) NPP-based water use efficiency ( $\text{WUE}_{\text{NPP}}$ ) is the ratio of NPP to ET. WUE for each individual grid cell was calculated as annual GPP or NPP in the grid cell divided by annual ET, as  $\text{WUE}_{\text{GPP}}$  or  $\text{WUE}_{\text{NPP}}$ . The area-weighted mean of variables (GPP, NPP and ET and WUE) were reported to represent the whole study domain. To measure the strength of future climate scenario effect, the linear changing trends over historical period (1900–2014) and projected simulation period (2015–2100) were quantified by the ordinary least square estimation, using a `regline_stats` function with NCL (NCAR Command Language, version 6.5.0, <https://www.ncl.ucar.edu/>). The Pearson correlation coefficient was calculated to analyze the sensitivity of WUE to GPP, NPP and ET by using a `escorc` function with the NCL.

### 3. Results

#### 3.1. Spatiotemporal pattern of GPP and NPP

CMIP6 simulations produced similar long-term trends for annual GPP and NPP, with slightly increasing trends during historical period (1900–2014) and strong increasing trends in projected period (2015–2100) (Fig. 2). On average, the annual GPP of 1900–2014 was  $340.24 \text{ g C m}^{-2} \text{ year}^{-1}$  in the study area, along with its increasing trend at  $1.08 \text{ g C m}^{-2} \text{ year}^{-2}$  ( $P < 0.05$ ) during this period. Annual NPP was averaged at  $201.81 \text{ g C m}^{-2} \text{ year}^{-1}$ , with a weak increasing trend at  $0.58 \text{ g C m}^{-2} \text{ year}^{-2}$  ( $P < 0.05$ ) over the whole historical period. High-emission scenario lead to higher changing rates of both GPP and NPP (Fig. 2). During the projected period of 2015 to 2100, the increasing rates of GPP are  $1.12 \text{ g C m}^{-2} \text{ year}^{-2}$ ,  $3.37 \text{ g C m}^{-2} \text{ year}^{-2}$ ,  $4.07 \text{ g C m}^{-2} \text{ year}^{-2}$ , and  $7.33 \text{ g C m}^{-2} \text{ year}^{-2}$  ( $P < 0.05$ ) under SSP126, SSP245, SSP460 and SSP585, respectively. The increasing rates in NPP are  $0.53 \text{ g C m}^{-2} \text{ year}^{-2}$ ,  $1.71 \text{ g C m}^{-2} \text{ year}^{-2}$ ,  $2.05 \text{ g C m}^{-2} \text{ year}^{-2}$ , and  $3.58 \text{ g C m}^{-2} \text{ year}^{-2}$  ( $P < 0.05$ ) under SSP126, SSP245, SSP460 and SSP585, respectively. The projected annual GPP and NPP under SSP585 increase to as high as  $1043.44 \text{ g C m}^{-2} \text{ year}^{-1}$  and  $551.24 \text{ g C m}^{-2} \text{ year}^{-1}$  in the 2090–2099 respectively, compared to the much lower magnitudes of  $577.25 \text{ g C m}^{-2} \text{ year}^{-1}$  and  $325.83 \text{ g C m}^{-2} \text{ year}^{-1}$  under SSP126 for annual GPP and NPP, respectively. In contrast with other projection experiments, both annual GPP and annual NPP cease increasing and even start to decline at the second half of the 21st century under SSP126 scenario. Meanwhile, the model outputs under SSP585 have higher uncertainties of GPP and NPP (Fig. 2) than the SSP126 scenario.

There are large spatial heterogeneities in both GPP and NPP for historical and future simulations (Fig. 3 and Fig. 4). The higher increases in GPP and NPP occur in the western and southeast of the study domain (mostly in China) (25% of the study area), and these areas also have the large variations among different scenarios. In central and eastern parts of the study domain (30% of the study area), both GPP and NPP show

relatively moderate variations under historical and future scenarios. By contrast, the GPP and NPP have the smallest variations among scenarios in most northern and southwest parts of the study domain (15% of the study area). Furthermore, substantial variations in GPP and NPP are observed under high-emission scenario. Under the SSP126 scenario, the high increases in GPP and NPP ( $720 \text{ g C m}^{-2} \text{ year}^{-1}$  for GPP and  $360 \text{ g C m}^{-2} \text{ year}^{-1}$  for NPP) occur in >23.9% or 37.3% of the study area during 2090s, compared to 26.1% or 42.4% in the 2050s, respectively, while the magnitudes of increase for GPP and NPP under SSP585 are from 52.2% to 82.6% and 64.6% to 86.6%, respectively, of the entire region.

#### 3.2. Spatiotemporal pattern of ET

Large variations were observed for ET across the study domain during 1900–2100. CMIP6 yields a mean annual ET of  $304.77 \text{ mm. year}^{-1}$  over the historical period, while larger values in the future for all projected experiments, with  $349.76 \text{ mm. year}^{-1}$ ,  $352.61 \text{ mm. year}^{-1}$ ,  $356.61 \text{ mm. year}^{-1}$ , and  $368.78 \text{ mm. year}^{-1}$  under SSP126, SSP245, SSP460 and SSP585, respectively (Fig. 5). Overall, it is observed that historical ET has a slight increase ( $0.12 \text{ mm. year}^{-2}$ ,  $P < 0.05$ ), but a rapid increase after 2000s ( $1.80 \text{ mm. year}^{-2}$ ,  $P < 0.05$ ). The increasing trends in annual ET during four projected experiments are larger than that in the historical period, and the larger increase occurred under high-emission scenario, with  $0.17 \text{ mm. year}^{-2}$ ,  $0.42 \text{ mm. year}^{-2}$ ,  $0.49 \text{ mm. year}^{-2}$ , and  $0.86 \text{ mm. year}^{-2}$  ( $P < 0.05$ ) under SSP126, SSP245, SSP460 and SSP585, respectively. But the increasing trends in ET under all scenarios diminish in the second half of the 21st century, especially under lower scenarios, and that under the lowest scenario (SSP126) even decrease in the end ( $-0.09 \text{ mm. year}^{-2}$ ,  $P < 0.05$ ). Meanwhile, the SDs in ET at the last 10 simulation years are  $10.57 \text{ mm. year}^{-1}$ ,  $10.90 \text{ mm. year}^{-1}$ ,  $14.81 \text{ mm. year}^{-1}$ , and  $33.61 \text{ mm. year}^{-1}$  under SSP126, SSP245, SSP460 and SSP585, respectively, implying the high uncertainty under high-emission scenario.

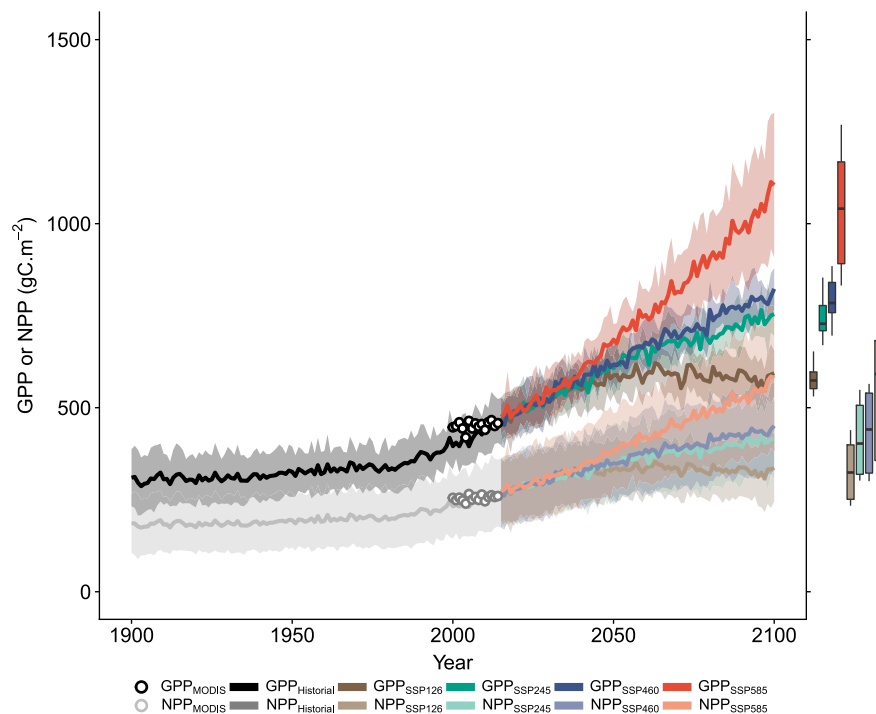


**Fig. 2.** Time series of annual GPP and NPP from 1900 to 2100. Dot indicates MODIS-derived data, while solid line indicates data from ESMs simulations. Different line colors indicate different CMIP6 experiments (Historical, SSP126, SSP245, SSP460 or SSP585) for each variable (GPP or NPP). The solid line under each CMIP6 experiment represents the three-ESM-model ensemble mean, and the corresponding shaded envelope represents the standard deviation. Box and whiskers (mean, one standard deviation, and minimum to maximum range) at the right side of the figure show the differences during the last 10 years among all three ESMs simulations.



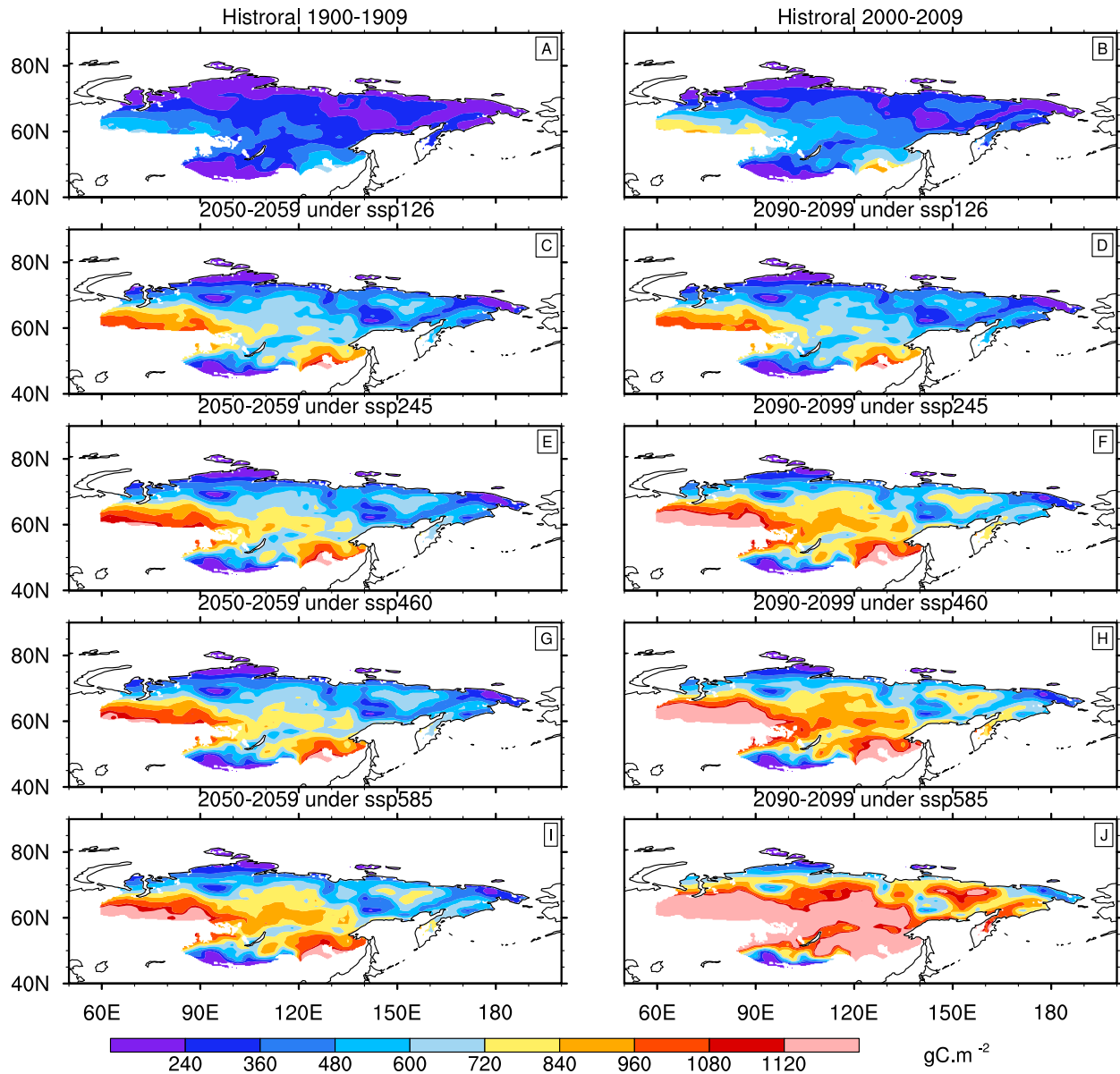


**Fig. 3.** Gridded CMIP6 ensemble mean GPP in Asian permafrost region under the historical experiment (A, B), and four scenarioMIP experiments: SSP126 (C, D), SSP245 (E, F), SSP460 (G, H) or SSP585 (I, J). Shown are the decades of 1900s, 2000s, 2050s, and 2090s as historical periods (A, 1900–1909; B, 2000–2009) and future periods (C, E, G, I, 2050–2059; D, F, H, J, 2090–2099). CMIP6 ensemble mean GPP at each grid cell is computed for each year and then time averaged all 10 years.

Spatial trends of ET for the decades of 1900s, 2000s, 2050s and 2090s show substantial heterogeneity in the study area (Fig. 6), although there is a slight difference among scenarios. All simulations present higher ET ( $>360 \text{ mm} \cdot \text{year}^{-1}$ ) in the southern areas and lower ET ( $<360 \text{ mm} \cdot \text{year}^{-1}$ ) in the northern areas. The CMIP6 simulations yield higher terrestrial water loss in the southern areas than that with historical experiment, but slight increase occurs in the areas of north  $70^\circ\text{N}$  and southwest corner. There is no large spatial difference between low-emission and moderate scenarios, but large difference from the SSP585 scenario. Moreover, no large spatial differences are found among specific periods (1900s and 2000s are for historical simulation, 2050s and 2090s are for projected simulations) of each independent experiment except the SSP585 scenario. Under the SSP585 scenario, the high increase in ET ( $>460 \text{ mm} \cdot \text{year}^{-1}$ ) will be in  $>17.1\%$  and  $28.5\%$  of the study area during 2050s and 2090s, respectively, while that level of increases for historical simulation and other scenarios keep approximately 13.5% of the study area during their corresponding periods.

### 3.3. Spatiotemporal pattern of WUE

Over the study period of 1900 to 2100, both annual  $\text{WUE}_{\text{GPP}}$  and  $\text{WUE}_{\text{NPP}}$  show increasing trends (Fig. 7), and their increases are lower over the historical period than during projection period regardless of climate change scenario. The average historical annual  $\text{WUE}_{\text{GPP}}$  is  $1.12 \text{ g C m}^{-2} \cdot \text{mm}^{-1}$ , comparing to  $\text{WUE}_{\text{NPP}}$  of  $0.67 \text{ g C m}^{-2} \cdot \text{mm}^{-1}$ . The historical increasing trends of  $\text{WUE}_{\text{GPP}}$  and  $\text{WUE}_{\text{NPP}}$  are  $0.0030 \text{ g C m}^{-2} \cdot \text{mm}^{-1} \cdot \text{year}^{-1}$  and  $0.0016 \text{ g C m}^{-2} \cdot \text{mm}^{-1} \cdot \text{year}^{-1}$ , respectively. The projected increasing rates of annual  $\text{WUE}_{\text{GPP}}$  under SSP126, SSP245, SSP460 and SSP585 are  $0.0025 \text{ g C m}^{-2} \cdot \text{mm}^{-1} \cdot \text{year}^{-1}$ ,  $0.0075 \text{ g C m}^{-2} \cdot \text{mm}^{-1} \cdot \text{year}^{-1}$ ,  $0.009 \text{ g C m}^{-2} \cdot \text{mm}^{-1} \cdot \text{year}^{-1}$  and  $0.0153 \text{ g C m}^{-2} \cdot \text{mm}^{-1} \cdot \text{year}^{-1}$ , respectively, while the increasing rates in annual  $\text{WUE}_{\text{NPP}}$  under those scenarios correspond to  $0.0011 \text{ g C m}^{-2} \cdot \text{mm}^{-1} \cdot \text{year}^{-1}$ ,  $0.0037 \text{ g C m}^{-2} \cdot \text{mm}^{-1} \cdot \text{year}^{-1}$ ,  $0.0044 \text{ g C m}^{-2} \cdot \text{mm}^{-1} \cdot \text{year}^{-1}$  and  $0.007 \text{ g C m}^{-2} \cdot \text{mm}^{-1} \cdot \text{year}^{-1}$ , respectively. But there are no significant increasing trends and even the trends

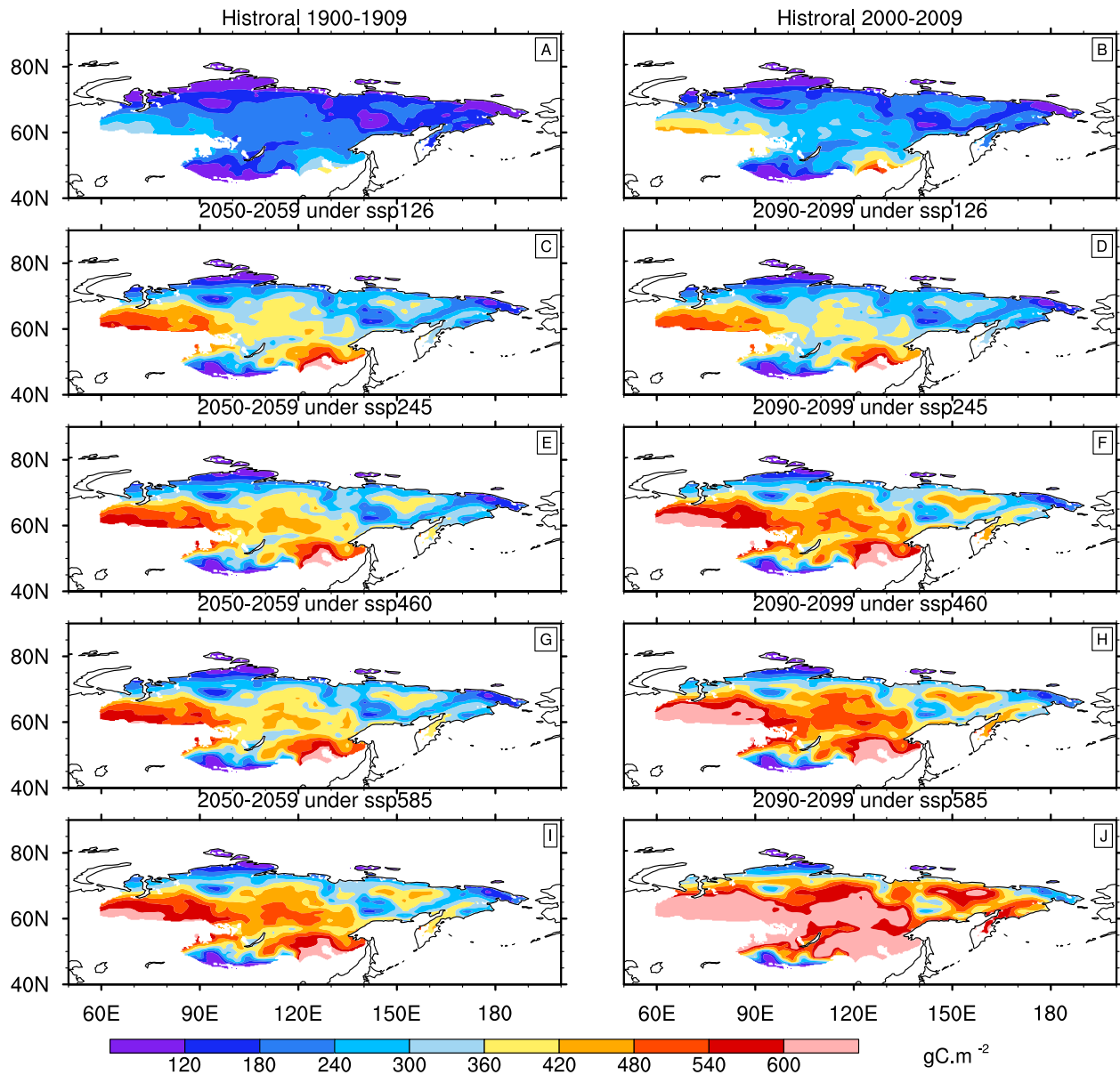


**Fig. 4.** Gridded CMIP6 ensemble mean NPP in Asian permafrost region under the historical experiment (A, B), and four scenarioMIP experiments: SSP126 (C, D), SSP245 (E, F), SSP460 (G, H) or SSP585 (I, J). Shown are two different 10-year periods for both historical periods (A, 1900–1909; B, 2000–2009) and future periods (C, E, G, I, 2050–2059; D, F, H, J, 2090–2099). CMIP6 ensemble mean NPP at each grid cell is computed for each year and then time averaged all 10 years.

start to decline in 2050 for SSP126, corresponding to the trends of GPP and NPP.

Different spatial patterns between historical and projected periods for both simulated  $WUE_{GPP}$  and  $WUE_{NPP}$  are found (Fig. 8 and Fig. 9). During the historical period, both  $WUE_{GPP}$  and  $WUE_{NPP}$  show slight variations in the study area. Above-average  $WUE_{GPP}$  ( $>1.12 \text{ g C m}^{-2} \text{ mm}^{-1}$ ) is observed in western, southeast and central areas (3.81% of the study area) in the 1900s and then extend to northern area in the 2000s (72.9% of the study area).  $WUE_{NPP}$  shows a similar spatial distribution with  $WUE_{GPP}$  from 1900s to 2000s; however, high  $WUE_{GPP}$  and  $WUE_{NPP}$  are observed across large area under severer scenarios. For example, under SSP585 areas with  $WUE_{GPP}$  of above  $2 \text{ g C m}^{-2} \text{ mm}^{-1}$  and  $WUE_{NPP}$  of above  $0.8 \text{ g C m}^{-2} \text{ mm}^{-1}$  occupy nearly 49.6% and 87.1% of the total area in 2050s, respectively, while those in 2090s are 85.9% and 94.0%, respectively. Both  $WUE_{GPP}$  and  $WUE_{NPP}$  show large spatial variabilities under all scenarios. They show large increases in western and northern parts, but the WUE values are small in southwest and eastern

parts of the study area. In central and southeast areas, the WUE shows moderate increases.

#### 3.4. Comparison between CMIP6 and MODIS

The CMIP6-simulated GPP, NPP, ET,  $WUE_{GPP}$  and  $WUE_{NPP}$  were evaluated with the MODIS-based data over the period 2000–2014. The temporal behavior of NPP for ESMs is consistent with MODIS data (Fig. 2). However, CMIP6 results showed underestimations for GPP and ET over 2000 to 2014 (Fig. 2 and Fig. 5), by  $-24.79 \text{ g C m}^{-2} \text{ year}^{-1}$  and  $-12.88 \text{ mm} \cdot \text{year}^{-1}$ , respectively. Those differences subsequently resulted in overestimates of  $WUE_{GPP}$  and  $WUE_{NPP}$  in CMIP6 (Fig. 7). The mean differences for annual  $WUE_{GPP}$  and  $WUE_{NPP}$  between CMIP6 simulations and MODIS data over 2000–2014 are  $0.05 \text{ g C m}^{-2} \text{ mm}^{-1}$  and  $0.04 \text{ g C m}^{-2} \text{ mm}^{-1}$ , respectively. Both CMIP6 and MODIS data from 2000 to 2014 show long-term increasing trends with positive slopes of the trendline

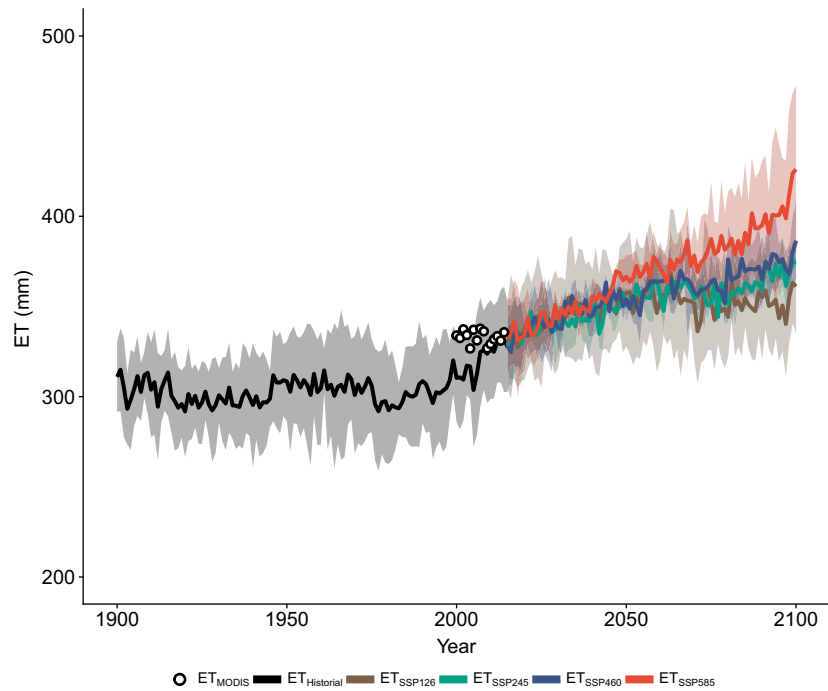


**Fig. 5.** Time series of annual ET in Asian permafrost region from 1900 to 2100. Dot indicates MODIS-derived data, while solid line indicates data from ESMs simulations. Different line colors indicate different CMIP6 experiments (Historical, SSP126, SSP245, SSP460 or SSP585) for ET. The solid line under each CMIP6 experiment represents the three-ESM-model ensemble mean, and the corresponding shaded envelope represents the standard deviation. Box and whiskers (mean, one standard deviation, and minimum to maximum range) at the right side of the figure show the differences during the last 10 years among all three ESMs simulations.

for all variables (except ET), although not obviously significant with MODIS data by  $P > .05$ . The increasing rates of CMIP6 results are larger than that with MODIS data. For example, CMIP6 simulations show an increasing rate of  $2.73 \text{ g C m}^{-2} \text{ year}^{-2}$  in NPP, compared to that of  $0.62 \text{ g C m}^{-2} \text{ year}^{-2}$  with MODIS. For ET, CMIP6 shows that the decadal change of ET is marked by an increasing trend ( $1.80 \text{ mm. year}^{-2}$ ), while a decreasing trend is presented with MODIS data ( $-0.12 \text{ mm. year}^{-2}$ ). Although these differences existed between CMIP6 and MODIS, both are consistent in terms of magnitudes (Figs. 2, 5, 7).

The spatial patterns from CMIP6 and MODIS agree reasonably well in the study area, although substantial differences in some areas (Fig. 10). Specifically, for GPP and NPP, good agreements are presented in most areas, even though CMIP6 showed slight overestimations in northern (42% of the study area) and slight underestimations in southern (51.7% of the study area) of the study domain. Compared to MODIS ET data, there is a good agreement for ET in northern area with CMIP6 simulations, while CMIP6 in most central and eastern areas (62.7% of the study area) have weaker ET and the simulations in some southern areas (29.7% of the study area) have a higher ET. There are significant spatial differences in  $\text{WUE}_{\text{GPP}}$  and  $\text{WUE}_{\text{NPP}}$  simulations (Fig. 10 D, E), which could also be implied from spatial heterogenic differences in GPP, NPP and ET between CMIP6 and MODIS. The good agreement for  $\text{WUE}_{\text{GPP}}$  occurs in the central area, and that for  $\text{WUE}_{\text{NPP}}$  is observed in northern areas. But CMIP6 simulate higher  $\text{WUE}_{\text{GPP}}$  in northern areas (32.7% of the study area) and lower  $\text{WUE}_{\text{GPP}}$  in majority of southern areas (59.2% of the study area). In contrast, there is only weaker  $\text{WUE}_{\text{NPP}}$  observed in CMIP6, whose large underestimations are found in most central and southern areas (95.2% of the study area). Overall, CMIP6-derived GPP and NPP are consistent with MODIS results for a majority of central areas, and CMIP6-derived ET estimation has good agreement in northern areas, while the simulations in central area and northern area have more reliability for  $\text{WUE}_{\text{GPP}}$  and  $\text{WUE}_{\text{NPP}}$ .

## 4. Discussion

### 4.1. Comparisons with previous studies

The CMIP6-based regional GPP, NPP, ET,  $\text{WUE}_{\text{GPP}}$  and  $\text{WUE}_{\text{NPP}}$  for the Asian permafrost region are comparable with previous estimations based on remote sensing, ESMs and integrated multi-source data (Table 1). A mean annual GPP, NPP and ET values from 1900 to 2014 of  $340.24 \text{ g C m}^{-2}$ ,  $201.81 \text{ g C m}^{-2}$  and  $304.77 \text{ mm}$ , respectively, are estimated in this study. These estimates are lower than the global mean value estimated by other researchers (Table 1), but still fall within reasonable range reported for the Asian region (Chen et al., 2017; Zhang et al., 2014a).  $\text{WUE}_{\text{NPP}}$  and  $\text{WUE}_{\text{GPP}}$  also fall in the ranges in other studies (Song et al., 2013; Chen et al., 2017; Guo et al., 2019), but much lower than the global estimates. The results that less carbon gain, water loss and water use efficiency in the Asian permafrost region than those in other regions are mainly attributed to temperature and solar radiation limitations to vegetations activity at high latitudes (Sun et al., 2016). Tang et al. (2014) found a distinct latitudinal trend in WUE of terrestrial ecosystems that WUE declines toward northern higher latitudes beyond  $51^\circ\text{N}$ , and they also highlighted the biological adaptations of WUE to climatic change.

In this study, the positive trend of carbon gain (GPP and NPP) are in line with many previous reports (Chen et al., 2017; Forkel et al., 2016; Zhu et al., 2016), in which high northern latitude regions experienced a continuous increasing terrestrial carbon sequestration caused by warming and extended growing season. The increasing trends of annual ET over historical and scenario periods are consistent with some earlier global studies (Brutsaert, 2006; Yan et al., 2013; Zeng et al., 2012; Zhang et al., 2015), and the general upward trends in  $\text{WUE}_{\text{GPP}}$  and  $\text{WUE}_{\text{NPP}}$  agree with the previous global studies by Chen et al. (2017) and Liu et al. (2020). But the increasing trends of carbon loss, ET and WUE are lower than other regions, mainly due to the different sensitivities of carbon loss, ET and WUE to climate and  $\text{CO}_2$  changes. Evidences for the positive impact of climate warming on vegetation growth and NPP have

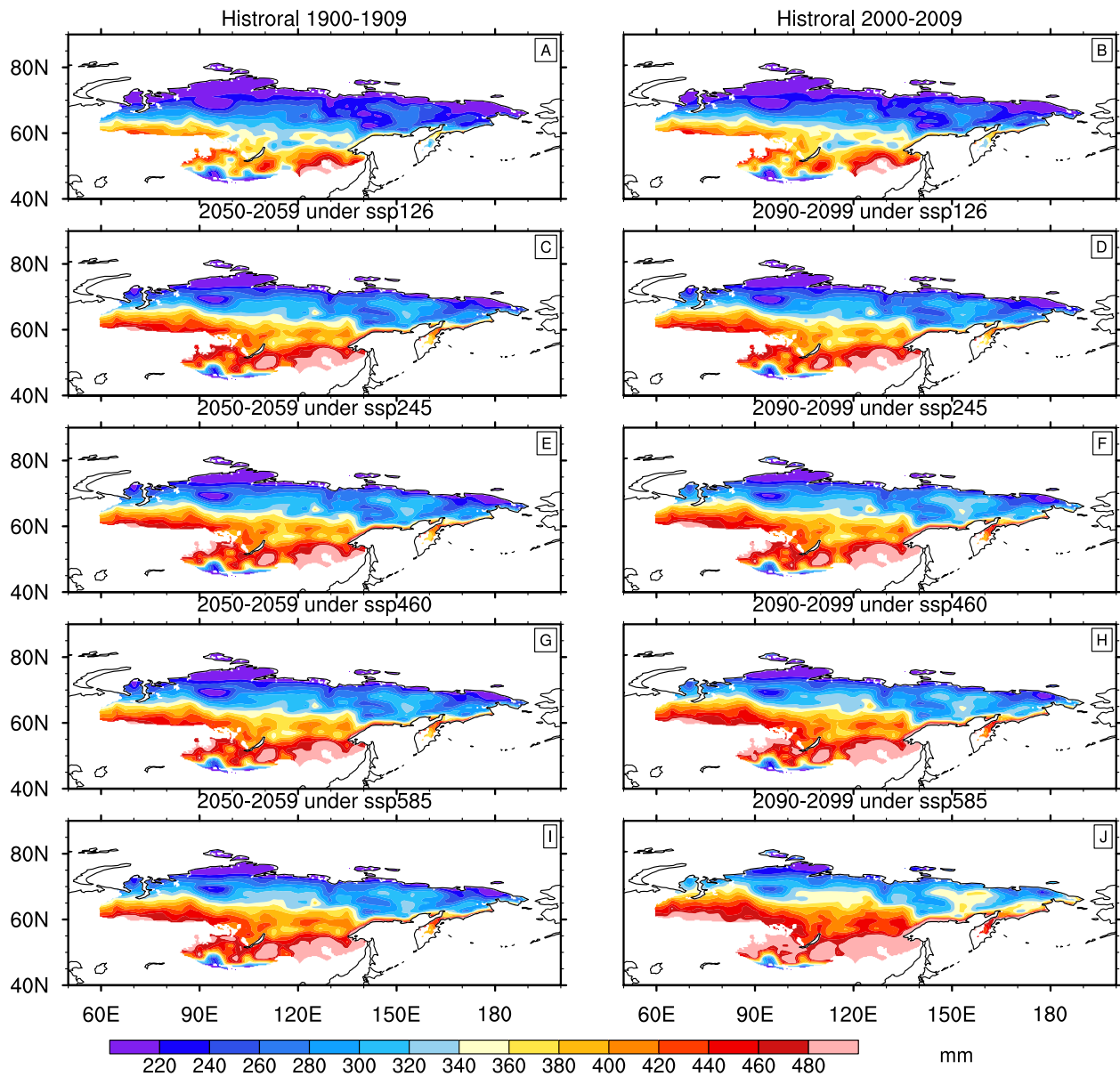


**Fig. 6.** Gridded CMIP6 ensemble mean ET in Asian permafrost region under the historical experiment (A, B), and four scenarioMIP experiments: SSP126 (C, D), SSP245 (E, F), SSP460 (G, H) or SSP585 (I, J). Shown are two different 10-year periods for both historical periods (A, 1900–1909; B, 2000–2009) and future periods (C, E, G, I, 2050–2059; D, F, H, J, 2090–2099). CMIP6 ensemble mean ET at each grid cell is computed for each year and then time averaged all 10 years.

been widely reported in permafrost regions (Xia et al., 2017). However, the impact of elevated CO<sub>2</sub> on NPP in northern permafrost regions is found to be positive (Grulke et al., 1990) or neutral (Korner et al., 1997; Oberbauer et al., 1986). And it is well known that vegetation production is more limited by nitrogen availability in tundra and boreal ecosystems than in temperate and tropical ecosystems (Koven et al., 2015; Luo et al., 2004; Reich et al., 2006).

However, there are still some discrepancies with a few studies that reported declining ET and WUE (Jung et al., 2010; Peterson et al., 1995) and others that found no trends (Badgley et al., 2015; Zhang et al., 2016). The discrepancies possibly stem from the uncertainties in our knowledge of how ET could vary with climate changing (Badgley et al., 2015), which further determines the changing trend in WUE. More specifically, ET decreases in some regions since latent heat fluxes are limited by moisture supply (Jung et al., 2010). In addition, terrestrial ET could be limited via plant regulation of stomatal closure (Rigden and Salvucci, 2017) and the water content of plant (Choat et al., 2018; Zhang et al., 2020), while several recent studies suggested elevated

atmospheric CO<sub>2</sub> may stimulate plant growth, thereby enhancing ET as larger leaf area (Zeng et al., 2012; Zhang et al., 2015; Zhang et al., 2016). Hence, our results of increasing ET may indicate that the increase of ET caused by the radiative effect and the vegetation greening may be larger than the ET reduction by vegetation physiological effect in the Asian permafrost region.

#### 4.2. Vegetation activity drives WUE

As a critical linkage of terrestrial carbon and water cycles, WUE quantifies the tradeoff between carbon gain and water loss. In the Asian permafrost region, GPP and NPP show significant increases, associated with the small increase in ET. Consequently, WUE show the continuous increase over the historical and future periods, which suggests a shift is occurring in the terrestrial water economics of carbon uptake as climate changing in this study area. The disproportionate change in carbon gain and water loss indicates that vegetation activity drives the water use efficiency in the Asian permafrost region. The stronger



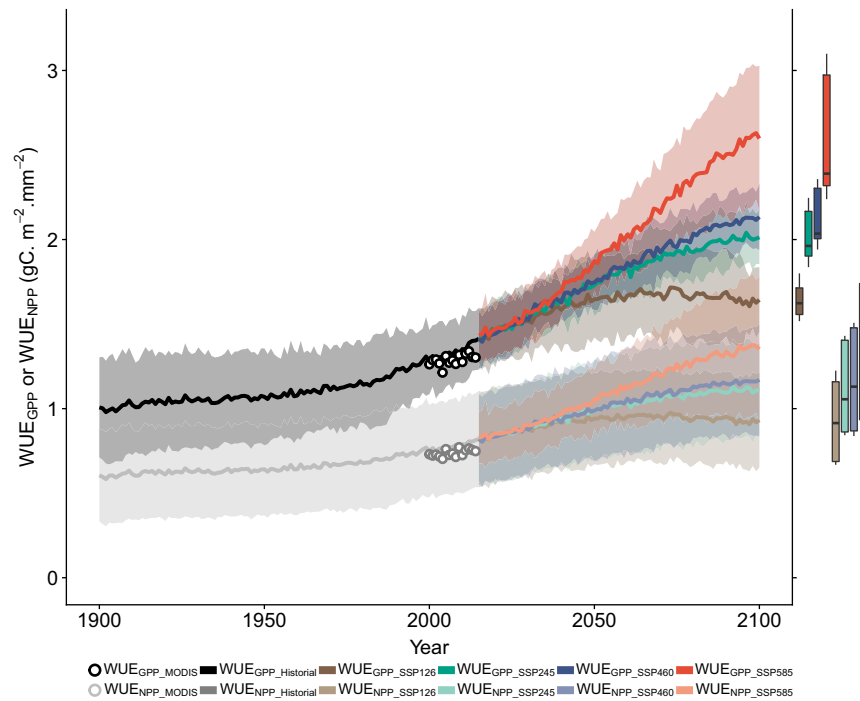


**Fig. 7.** Time series of annual  $WUE_{GPP}$  and  $WUE_{NPP}$  from 1900 to 2100. Dot indicates MODIS-derived data, while solid line indicates data from ESMs simulations. Different line colors indicate different CMIP6 experiments (Historical, SSP126, SSP245, SSP460 or SSP585) for  $WUE_{GPP}$  or  $WUE_{NPP}$ . The solid line under each CMIP6 experiment represents the three-ESM-model ensemble mean, and the corresponding shaded envelope represents the standard deviation. Box and whiskers (mean, one standard deviation, and minimum to maximum range) at the right side of the figure show the differences during the last 10 years among all three ESMs simulations.

relationships between carbon gain and WUE than between ET and WUE further confirm that the response of WUE to climate change was mainly determined by the vegetation carbon acclimation, rather than the water loss (Fig. 11). Generally, both  $WUE_{GPP}$  and  $WUE_{NPP}$  have high Pearson's correlation coefficients with GPP and NPP in large areas of the Asian over the historical and future periods, respectively. Above 92% of the study domain under all scenarios shows more positive Pearson's correlation coefficients between the WUE and carbon gain than that between WUE and water loss. As expected, the domination of vegetation activity in contribution to WUE is getting stronger under high climate change scenarios, although the Pearson's correlation coefficients between WUE and carbon gain under the lowest scenarios (SSP126) is lower than historical period (Fig. 11).

At the global scale, terrestrial carbon uptake as the largest contributor to the increasing trends in WUE was also suggested in many previous studies. For example, Cheng et al. (2017) found mean annual global ET increased little during 1982–2011 at about 2%, while global GPP increased significantly at about 17%. Huang et al. (2015) reported the increase in WUE is due to the stimulated GPP but no change in ET under future warming. At the regional scale, Liu et al. (2020) also suggested the increase in WUE from 1982 to 2011 in the boreal Eurasia region mainly contributed toward the increase in GPP using multi-model ensemble data. There are probably two main reasons for the rising domination of vegetation activity to the enhancement of WUE in the study. First, air temperature had a high increase trend ( $0.02\text{ }^{\circ}\text{C}\cdot\text{year}^{-1}$ ,  $P < 0.05$ ) over 1900 to 2014 (Fig. S1). Vegetation carbon accumulation is more sensitive to climate change than ET (Forkel et al., 2016; Jin et al., 2017; White et al., 1999), mainly due to the stronger direct impacts of  $\text{CO}_2$  fertilization and warming and stronger indirect impacts of the length of a growing season on photosynthesis in the northern high latitudes (Forkel et al., 2016; Zhu et al., 2016). The second possible mechanism is the warming-induced soil moisture supply limitation in this study area (Fig. S2), which could cause the lower increase in ET (Jung et al., 2010; Liu et al., 2020), and the important role in stomatal regulation could reduce water loss by stomata closure at high vapor

pressure deficit under warming (Rigden and Salvucci, 2017), especially in the water-limitation area in southwestern parts of our study domain.

#### 4.3. CUE explains WUE variations

The pattern of NPP/GPP ratio, or carbon use efficiency (CUE), explains the differences in trends between GPP and NPP,  $WUE_{GPP}$  and  $WUE_{NPP}$  well in this study area. The results showed annual NPP increased by  $0.58\text{ g C m}^{-2}\cdot\text{year}^{-1}$  in the study area over 1900–2014, which is much lower than annual GPP at  $1.08\text{ g C m}^{-2}\cdot\text{year}^{-1}$ . Likewise, annual GPP-based WUE ( $0.0030\text{ g C m}^{-2}\cdot\text{mm}^{-1}\cdot\text{year}^{-1}$ ) also show more significantly increasing trend than NPP-based WUE ( $0.0016\text{ g C m}^{-2}\cdot\text{mm}^{-1}\cdot\text{year}^{-1}$ ) over the same period. The CUE reflects the fraction of assimilated carbon allocated to autotrophic respiration and represents how efficient an ecosystem is for investing assimilated carbon for growth (Waring et al., 1998), and is essential for advancing our knowledge of global terrestrial carbon cycling and its response to ongoing climate change (Xia et al., 2017; Zhang et al., 2014b). GPP has high increasing trend during 1900–2014, whereas the increase in NPP is weak, leading to a decreasing CUE in this study area (Fig. S3). Hence, climate change occurred in the Asian permafrost region is suppressing the partition of plant assimilated carbon into growth. Zhang et al., 2014b found the global CUE exhibited a spatial pattern closely associated with climate, and the areas with decreasing CUE were primarily located in central Asia and high latitude zones in west Asia, with simultaneous increasing temperatures and decreasing precipitation. In contrast, annual precipitation in our study area presents a slightly increasing trend ( $0.42\text{ mm}\cdot\text{year}^{-1}$ ,  $P < 0.05$ ) over 1900 to 2014 (Fig. S2), although the annual air temperature is rising (Fig. S1). In addition, the mean historical CUE in this study area is near 0.6, which is higher than Amazonian forest of 0.36 (Rowland et al., 2014) and temperate forest of 0.5 (Waring et al., 1998).

The high NPP/GPP ratio estimates in this study area agree with many previous studies. For example, Ise et al. (2010) also reported the CUE was highest in boreal forests (0.54–0.57) and lowest in

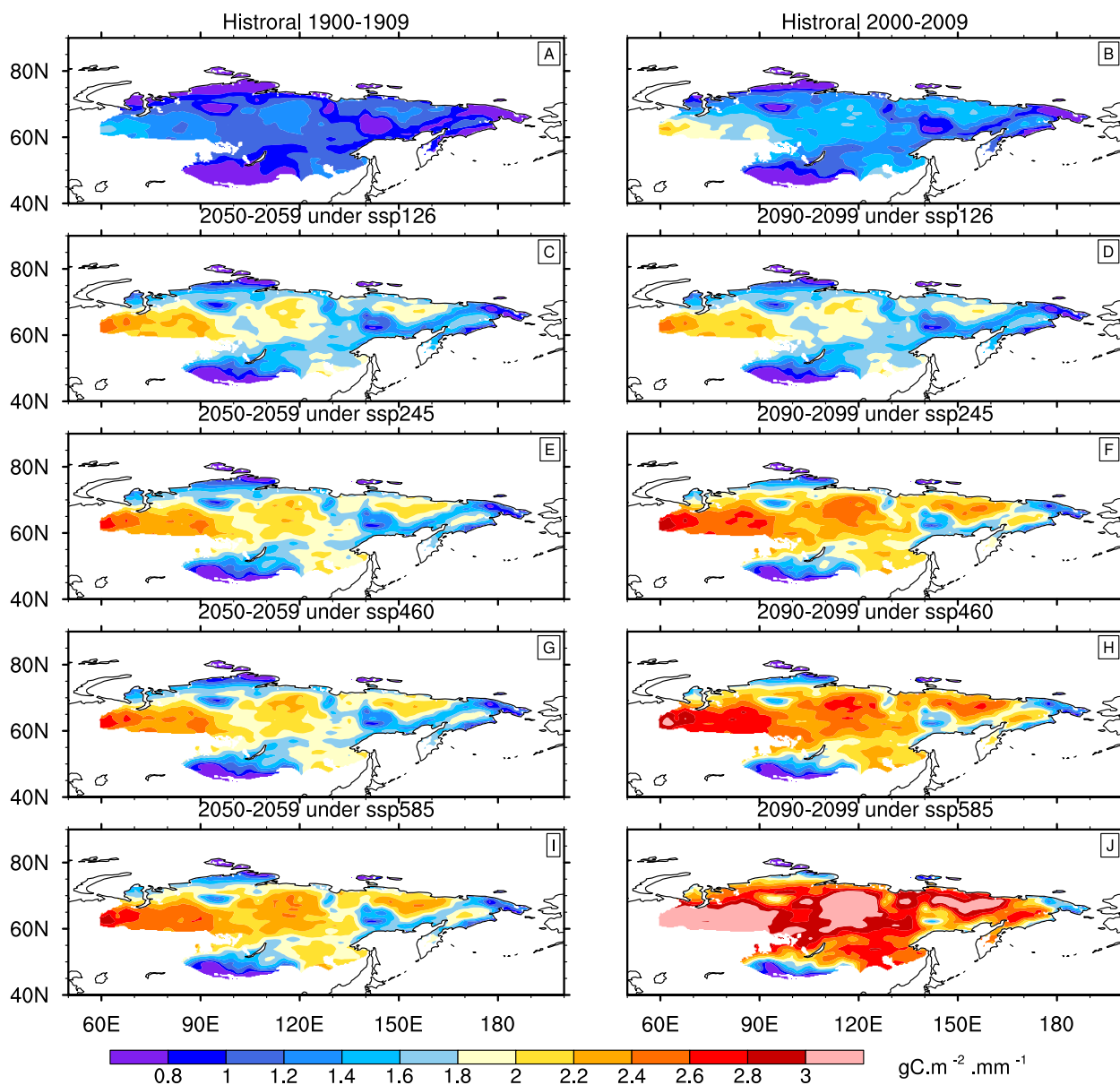


**Fig. 8.** Gridded CMIP6 ensemble mean  $WUE_{GPP}$  in Asian permafrost region under the historical experiment (A, B), and four scenarioMIP experiments: SSP126 (C, D), SSP245 (E, F), SSP460 (G, H) or SSP585 (I, J). Shown are two different 10-year periods for both historical periods (A, 1900–1909; B, 2000–2009) and future periods (C, E, G, I, 2050–2059; D, F, H, J, 2090–2099). CMIP6 ensemble mean  $WUE_{GPP}$  at each grid cell is computed for each year and then time averaged all 10 years.

tropical forests (0.43–0.44) with ecosystem model estimates. Bloom et al. (2016) reported the highest CUE of 0.49–0.50 in global high-latitude ( $>55^\circ$  N/S) areas, based on model and satellite-based data. With MODIS-derived NPP and GPP data over 2000 to 2009, Zhang et al., 2014b also found the high CUE in a large part of Eurasia. The high CUE in this study suggests that the vegetation in the Asian permafrost region is much efficient at investing carbon. However, high uncertainty related to estimated carbon gain and CUE should not be ignored, and Xia et al. (2017) argued an overestimation of as high as 54% CUE from many terrestrial ecosystem models existed in the northern permafrost regions as compared to observations, mainly due to the divergent simulations of maintenance and growth respiration among models.

#### 4.4. Implication

The Asian permafrost region is a key component of global permafrost, embracing approximately 53% of the Northern Hemisphere's

total permafrost area. It is likely that this large soil carbon storage will be transferred to the atmosphere under climate change, with an accelerating rate (Schuur et al., 2008). However, one important offset to permafrost carbon losses is an increase in carbon uptake from the atmosphere by plant photosynthesis (Chapin III et al., 2011), since warmer temperatures and elevated  $CO_2$  stimulate photosynthetic rates (Jin et al., 2017; White et al., 1999), and lengthen the growing season (Forkel et al., 2016; Zhu et al., 2016). In our study, the increasing trends of GPP and NPP suggest the soil carbon losses in the Asian permafrost region will likely be cancelled out by the rising vegetation carbon sequestration, with the shift in vegetation water economics of carbon uptake. In addition, it should also be noted that the different algorithms for computing GPP and ET between ESMs and MODIS imply that there are still uncertainties in the ESM structures or parameter values, especially for the model results of GPP and ET. This may lead to underestimations of regional and global GPP and ET, when CMIP6 is applied to the assessments of carbon sequestration and water loss.

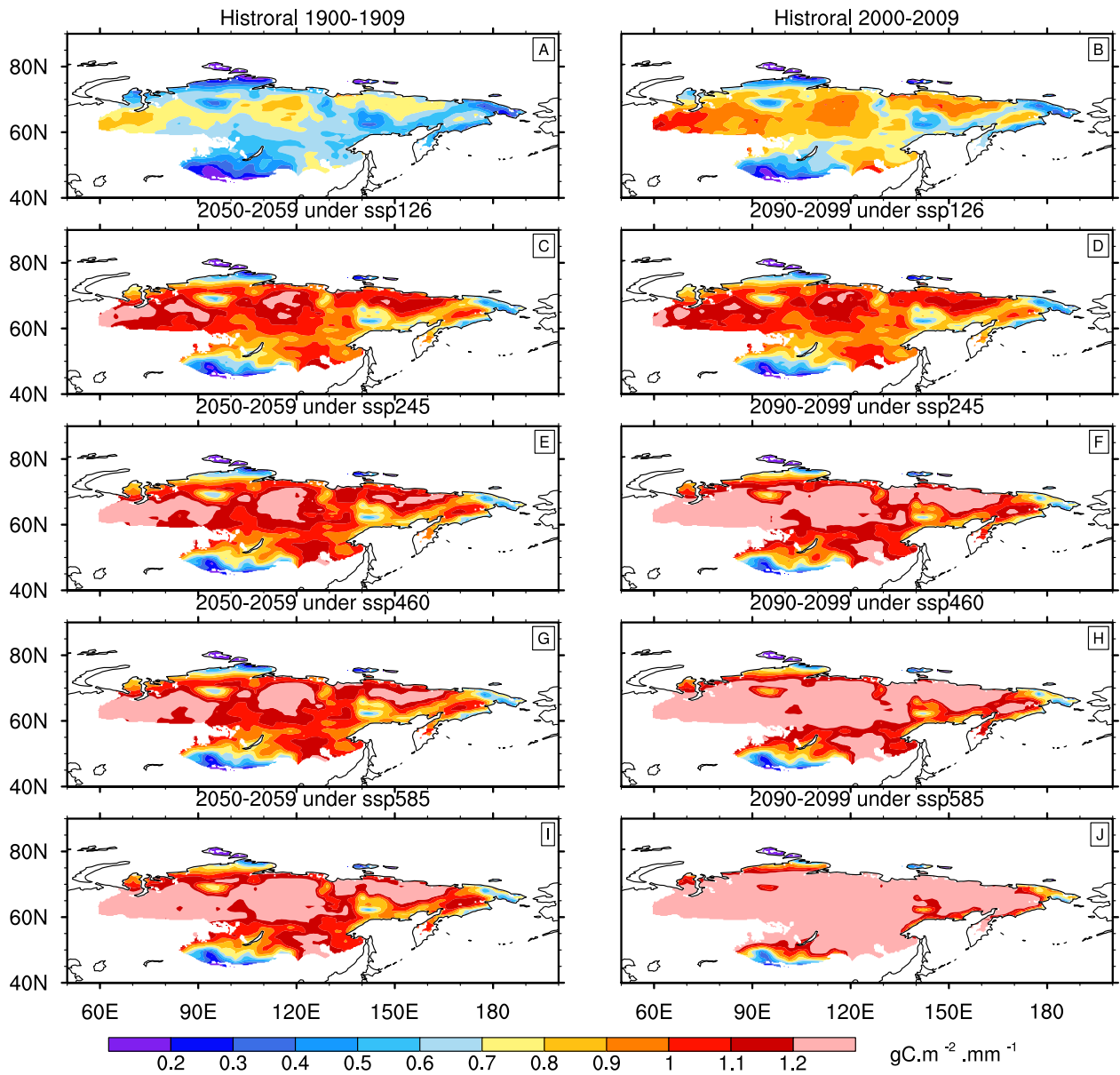


**Fig. 9.** Gridded CMIP6 ensemble mean  $WUE_{NPP}$  in Asian permafrost region under the historical experiment (A, B), and four scenarioMIP experiments: SSP126 (C, D), SSP245 (E, F), SSP460 (G, H) or SSP585 (I, J). Shown are two different 10-year periods for both historical periods (A, 1900–1909; B, 2000–2009) and future periods (C, E, G, I, 2050–2059; D, F, H, J, 2090–2099). CMIP6 ensemble mean  $WUE_{NPP}$  at each grid cell is computed for each year and then time averaged all 10 years.

#### 4.5. Future work

This study found that the rising vegetation activity dominates the growing WUE for the Asian permafrost region during 1900–2100; a few improvements are identified for our future work. Firstly, factors such as  $CO_2$  concentrations, air temperature and precipitation may also play important roles in the regional carbon sequestration and water loss. For example, previous studies attributed the decreasing ET in semiarid areas to increasing atmospheric demand (Yang et al., 2019). In fact, a small fraction of the land in study area is dominated by semiarid climate, which might have weakened the rising ET observed across the study region. Less is known for the semi-arid region and its mechanisms in this study. Secondly, plant functional types, nitrogen availability, soil physical and chemical properties and impact of land-use change are very important to the permafrost regions (Schuur et al., 2015). Hence, it is critical to further investigate the relative effects of multiple influential factors on the carbon and water cycle in this

study area, including climatic controls and the direct effect of biotic factors.

Thirdly, despite the model evaluation generally showed that the CMIP6 had reasonable representations of NPP for this study area, by the cross validation for CMIP6 model outputs with MODIS-derived data, current understanding about the long-term change in carbon and water cycle under future climate change is still very limited and depends largely on earth system models. The sources of uncertainty in the models, such as complex parameterization and the inaccuracy of input data, should be further addressed. Moreover, further improvement of model evaluation data quality should not be ignored. For example, the MODIS products are largely influenced by the performance of the algorithm, which are dependent on the accuracy of land cover, LAI, and meteorological data (Gebremichael and Barros, 2006; Guan et al., 2018; Sjostrom et al., 2013; Zhao et al., 2006; Zhao et al., 2005). Methane is another important carbon cycling process in the permafrost region and it becomes more and

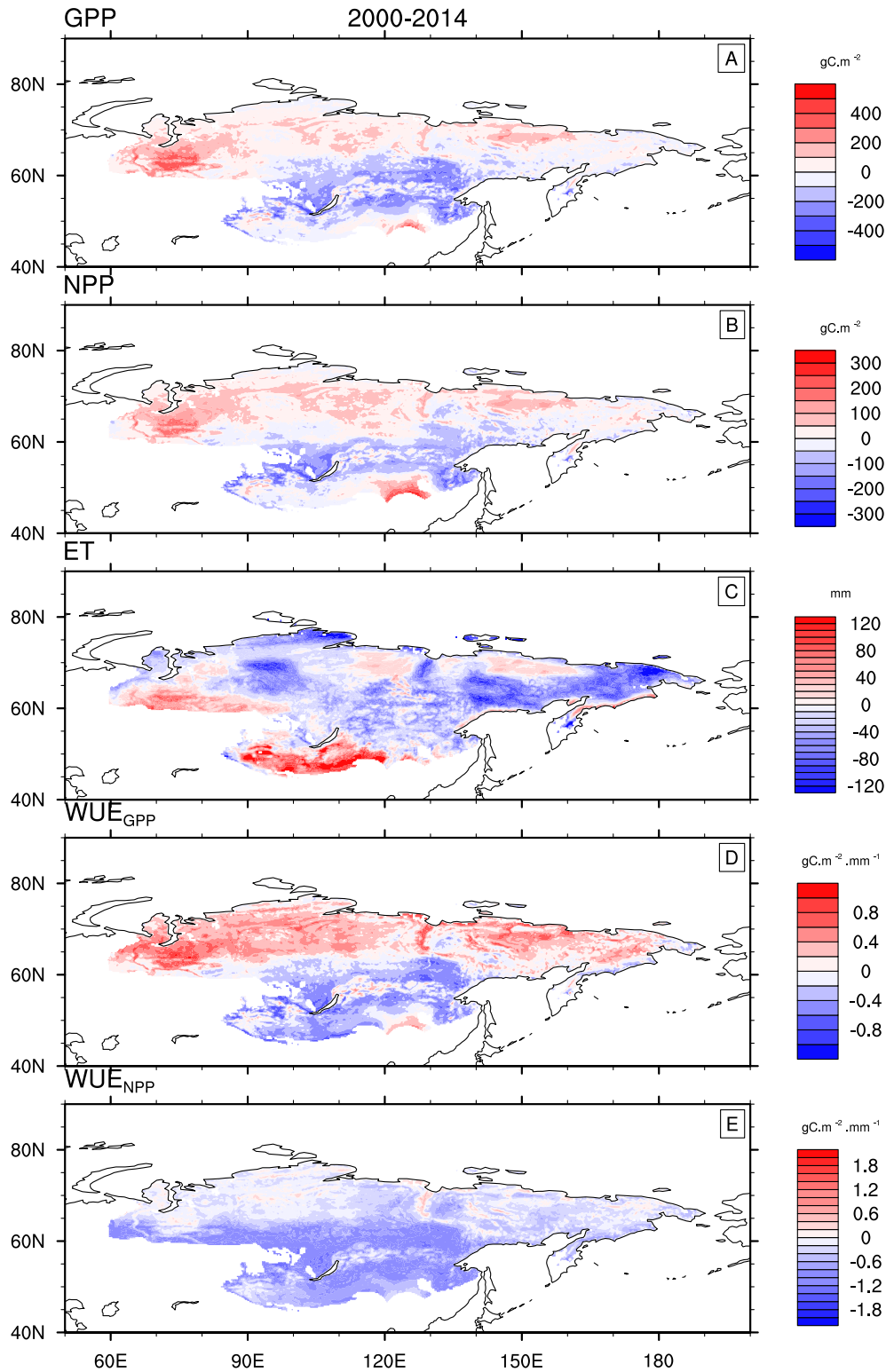


**Fig. 10.** Gridded GPP (A), NPP (B), ET (C),  $WUE_{GPP}$  (D) and  $WUE_{NPP}$  (E) differences in Asian permafrost region between CMIP6 simulations and MODIS data during 2000–2014. All variables were averaged for 15 years. CMIP6 simulations were three ESMs ensemble mean.

more important as climate warms (Knoblauch et al., 2018; Xu et al., 2015; Wang et al., 2019); improvements in land surface models (Xu et al., 2016) and manipulative experiments (Lupascu et al., 2012) should provide more reliable estimate and projection for carbon cycling in the permafrost region.

## 5. Conclusions

This study reported the spatiotemporal variations in GPP, NPP, ET, and WUE for the Asian permafrost region based on the CMIP6 simulations of 1900–2100. The simulated GPP, NPP, ET,  $WUE_{GPP}$ , and  $WUE_{NPP}$



**Table 1**

Synthesis of global and regional mean annual GPP, NPP, ET, and WUE and their trends based on MODIS data and ESMs simulations.

Location	Method	Period	GPP (g C m <sup>-2</sup> . yr <sup>-1</sup> )	NPP (g C m <sup>-2</sup> . yr <sup>-1</sup> )	ET (mm. yr <sup>-1</sup> )	WUE <sub>GPP</sub> (g C m <sup>-2</sup> . mm <sup>-1</sup> )	WUE <sub>NPP</sub> (g C m <sup>-2</sup> . mm <sup>-1</sup> )	GPP Changing Trend (g C m <sup>-2</sup> . yr <sup>-2</sup> )	NPP Changing Trend (g C m <sup>-2</sup> . yr <sup>-2</sup> )	ET Changing Trend (mm. yr <sup>-2</sup> )	WUE <sub>GPP</sub> Changing Trend (g C m <sup>-2</sup> . mm <sup>-1</sup> . yr <sup>-1</sup> )	WUE <sub>NPP</sub> Changing Trend (g C m <sup>-2</sup> . mm <sup>-1</sup> . yr <sup>-1</sup> )	References
Globe	MODIS	2000–2014				1.7							Huang et al. (2017)
Globe	MODIS	2000–2013				1.71					–0.0045		Tang et al. (2014)
Globe	MODIS	2000–2013	860.41–901.13		511.66–530.2	1.66–1.75					0.0025		Xue et al. (2015)
Globe	Ground-based +MODIS	1982–2011				2.1		–4.4–27.2			–0.0066–0.0513		Cheng et al. (2017)
Globe	Modeled data	2000–2009			549.25								Pan et al. (2015)
Globe	Integrated Data*	1989–1995			580								Mueller et al. (2011)
Globe	Integrated Data	1998–2008								0			Jung et al. (2010)
Globe	Integrated Data	1982–2009			558–650					1.1			Zeng et al. (2012)
Globe	Modeled data	1981–2012								0.54			Zhang et al. (2016)
Globe	Modeled data	1982–2011								0.45			Yan et al. (2013)
Globe	MODIS	2000–2012		448.97	520.05		0.868						Xia et al. (2015)
Globe	MODIS	2000–2010				1.8							Sun et al. (2016)
Globe	Modeled data	2000–2010				2							Sun et al. (2016)
Northern permafrost region	Modeled data	1960–2009	380–800	198–434									Xia et al. (2017)
Boreal	MODIS	2000–2010				1.6							Sun et al. (2016)
Boreal	Modeled data	2000–2010				2.2							Sun et al. (2016)
Eurasia	Integrated Data	2000–2009	470										Rawlins et al. (2015)
Europe	MODIS	2000–2012					1.130						Xia et al. (2015)
Asia	MODIS	2000–2012					0.739						Xia et al. (2015)
Northern China	Modeled data	2000–2005		153.26									Xing et al. (2010)
Mongolia	Modeled data	2000–2005		125.33									Xing et al. (2010)
Inner Mongolia	Modeled data	1982–2009			about 210								Li et al. (2012)
Eurasian Steppe	Modeled data	1999–2008		39.16–212.3	175.65–335.7		0.22–0.88						Chen et al. (2017)
East Asian	Modeled data	1982–2006			243	1.53–1.83							Zhang et al., 2014a
Eastern Kazakhstan	Modeled data	2004		168									Propastin and Kappas (2012)
Europe	Integrated Data	1982–2008								–0.009			Jung et al. (2010)
Europe	Integrated Data	1982–2009								0.96			Zeng et al. (2012)
Asia	Integrated Data	1982–2008								0.183			Jung et al. (2010)
Asia	Integrated Data	1982–2009								0.87			Zeng et al. (2012))
Asia	MODIS	2000–2014	450.99	254.46	332.98	1.29	0.74	0.8	0.62	–0.12	0.0038	0.0026	This Study
Asia	CMIP6	2000–2014	426.2	248.14	320.1	1.33	0.78	5.12	2.72	1.8	0.0083	0.0041	This Study
Asia	CMIP6	1900–2014	323.33	192.35	300.95	1.08	0.65	0.8	0.45	0.14	0.0021	0.0011	This Study

\* Integrated Data means the data were obtained from a combination of observations and simulations.

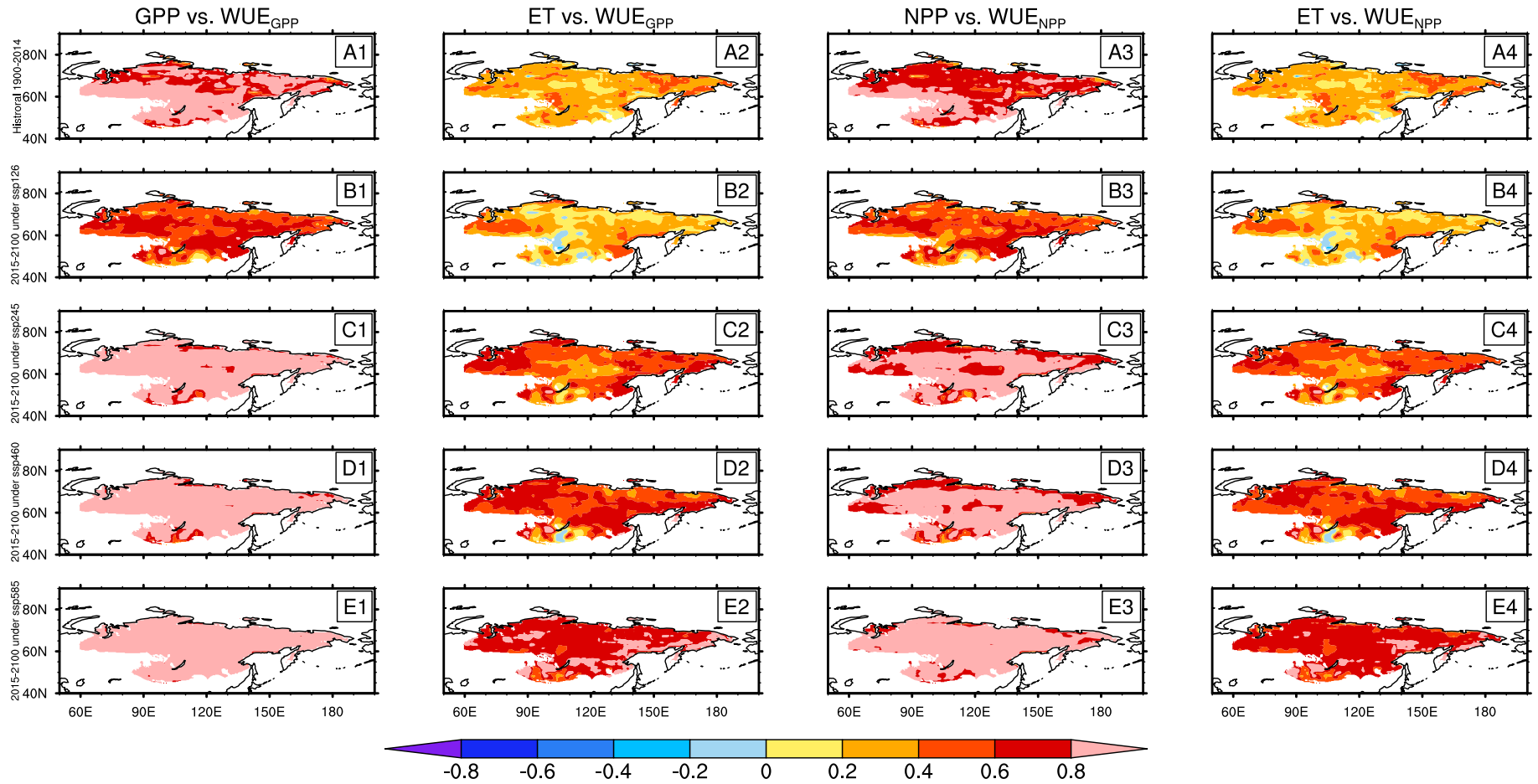


**Fig. 11.** Spatial map of Pearson's correlation coefficients between GPP, ET and  $WUE_{GPP}$ , and between NPP, ET and  $WUE_{NPP}$  in Asian permafrost region over 1900–2100 under different CMIP6 experiments: Historical (1900–2014, A1–B4), SSP126 (2015–2100, B1–B4), SSP245 (2015–2100, C1–C4), SSP460 (2015–2100, D1–D4) and SSP585 (2015–2100, E1–E4). The analysis was derived from time averages for each experiment period among three ESMs.

show slight increasing trends during historical period (1900–2014) and strong increasing trends in projection period (2015–2100), and projected impacts of climate change on all variables are greater under high-emission scenarios. There are larger increases in GPP, NPP and ET in western, central and southeast areas of this region, same spatial patterns were observed for WUE ( $WUE_{GPP}$  and  $WUE_{NPP}$ ). Additionally, comparing to MODIS-derived GPP, NPP, ET, and WUE during 2000–2014, the ESMs participated in CMIP6 yields the consistent results for NPP, while slightly underestimates GPP and ET, thus slightly overestimates  $WUE_{GPP}$  and  $WUE_{NPP}$ .

The finding that vegetation activity dominates the growing WUE in the Asian permafrost region implies the efficiency of permafrost region in trading water for carbon in the changing environment. Given that the hydrology is a key control on permafrost carbon cycling, the WUE patterns across space and time reported in this study provide valuable information for projecting permafrost dynamic under the changing climate.

### Declaration of competing interests

The authors declare that they have no known competing financial interests or personal relationships that could have appeared to influence the work reported in this paper.

### CRediT authorship contribution statement

**Fenghui Yuan:** Conceptualization, Data curation, Writing - original draft, Writing - review & editing. **Jianzhao Liu:** Data curation, Visualization. **Yunjiang Zuo:** Data curation, Visualization. **Ziyu Guo:** Methodology. **Nannan Wang:** Writing - review & editing. **Changchun Song:** Funding acquisition. **Zongming Wang:** Writing - review & editing. **Li Sun:** Writing - review & editing. **Yuedong Guo:** Methodology. **Yanyu Song:** Writing - review & editing. **Dehua Mao:** Writing - review & editing. **Feifan Xu:** Software. **Xiaofeng Xu:** Supervision.

### Acknowledgements

This study was partially supported by the National Key R&D Program [grant number 2016YFA0602303]; the “Top Notch” program and the National Natural Science Foundation of China [grant numbers 41730643, 31971728]. X.X. and F.Y. are grateful for financial and facility supports from San Diego State University and Northeast Institute of Geography and Agroecology, Chinese Academy of Sciences. The authors acknowledge the World Climate Research Programme's (WCRP's) Working Group on Coupled Modelling (WGCM), which is responsible for CMIP6, and also thank the climate modeling groups for producing and making available their model output, the Earth System Grid Federation (ESGF) for archiving the data and providing access, and the multiple funding agencies who support CMIP6 and ESGF.

### Appendix A. Supplementary data

Supplementary data to this article can be found online at <https://doi.org/10.1016/j.scitotenv.2020.139587>.

### References

- Badgley, G., Fisher, J.B., Jimenez, C., Tu, K.P., Vinukollu, R., 2015. On uncertainty in global terrestrial evapotranspiration estimates from choice of input forcing datasets. *J. Hydrometeorol.* 16 (4), 1449–1455. <https://doi.org/10.1175/jhm-d-14-0040.1>.
- Bloom, A.A., Exbrayat, J.F., van der Velde, I.R., Feng, L., Williams, M., 2016. The decadal state of the terrestrial carbon cycle: global retrievals of terrestrial carbon allocation, pools, and residence times. *Proc. Natl. Acad. Sci. U. S. A.* 113 (5), 1285–1290. <https://doi.org/10.1073/pnas.1515160113>.
- Boucher, O., Denvil, S., Caubel, A., Foujols, M.A., 2018. IPSL IPSL-CM6A-LR Model Output Prepared for CMIP6 CMIP. Version 20190130. Earth System Grid Federation <https://doi.org/10.22033/ESGF/CMIP6.1534>.
- Bring, A., Fedorova, I., Dibike, Y., Hinzman, L., Mard, J., Mernild, S.H., Prowse, T., Semenov, O., Stuefer, S.L., Woo, M.K., 2016. Arctic terrestrial hydrology: a synthesis of processes, regional effects, and research challenges. *J. Geophys. Res.-Biogeo.* 121 (3), 621–649. <https://doi.org/10.1002/2015jg003131>.
- Brown, J., Ferrians Jr., O., Heginbottom, J., Melnikov, E., 2002. *Circum-Arctic Map of Permafrost and Ground-Ice Conditions*, Version 2. 2. NSIDC: National Snow and Ice Data Center, Boulder, Colorado USA.
- Brutsaert, W., 2006. Indications of increasing land surface evaporation during the second half of the 20th century. *Geophys. Res. Lett.* 33 (20). <https://doi.org/10.1029/2006gl027532>.
- Chapin III, F.S., Matson, P.A., Vitousek, P.M., 2011. *Principles of Terrestrial Ecosystem Ecology*. 2nd edition. Springer, New York.
- Chen, Y.Z., Li, J.L., Ju, W.M., Ruan, H.H., Qin, Z.H., Huang, Y.Y., Jeelani, N., Padarian, J.A., Propastin, P., 2017. Quantitative assessments of water-use efficiency in Temperate Eurasian Steppe along an aridity gradient. *PLoS One* 12 (7). <https://doi.org/10.1371/journal.pone.0179875>.
- Cheng, L., Zhang, L., Wang, Y.P., Canadell, J.G., Chiew, F.H.S., Beringer, J., Li, L.H., Miralles, D.G., Piao, S.L., Zhang, Y.Q., 2017. Recent increases in terrestrial carbon uptake at little cost to the water cycle. *Nat. Commun.* 8. <https://doi.org/10.1038/s41467-017-00114-5>.
- Choat, B., Brodribb, T.J., Brodersen, C.R., Duursma, R.A., Lopez, R., Medlyn, B.E., 2018. Triggers of tree mortality under drought. *Nature* 558 (7711), 531–539. <https://doi.org/10.1038/s41586-018-0240-x>.
- Euskirchen, E.S., McGuire, A.D., Chapin, F.S., Yi, S., Thompson, C.C., 2009. Changes in vegetation in northern Alaska under scenarios of climate change, 2003–2100: implications for climate feedbacks. *Ecol. Appl.* 19 (4), 1022–1043. <https://doi.org/10.1890/08-0806.1>.
- Eyring, V., Bony, S., Meehl, G.A., Senior, C.A., Stevens, B., Stouffer, R.J., Taylor, K.E., 2016. Overview of the coupled model intercomparison project phase 6 (CMIP6) experimental design and organization. *Geosci. Model Dev.* 9 (5), 1937–1958. <https://doi.org/10.5194/gmd-9-1937-2016>.
- Forkel, M., Carvalhais, N., Rodenbeck, C., Keeling, R., Heimann, M., Thonicke, K., Zaehle, S., Reichstein, M., 2016. Enhanced seasonal CO<sub>2</sub> exchange caused by amplified plant productivity in northern ecosystems. *Science* 351 (6274), 696–699. <https://doi.org/10.1126/science.aac4971>.
- Friedl, M.A., Sulla-Menashe, D., Tan, B., Schneider, A., Ramankutty, N., Sibley, A., Huang, X., 2010. MODIS Collection 5 Global Land Cover: Algorithm Refinements and Characterization of New Datasets, 2001–2012, Collection 5.1 IGBP Land Cover. Boston University, Boston, MA, USA.
- Gebremichael, M., Barros, A.P., 2006. Evaluation of MODIS gross primary productivity (GPP) in tropical monsoon regions. *Remote Sens. Environ.* 100 (2), 150–166.
- Grunke, N.E., Riechers, G.H., Oechel, W.C., Hjelm, U., Jaeger, C., 1990. Carbon balance in tussock tundra under ambient and elevated atmospheric CO<sub>2</sub>. *Oecologia* 83 (4), 485–494. <https://doi.org/10.1007/bf00317199>.
- Guan, X., Shen, H., Li, X., Gan, W., Zhang, L., 2018. Climate control on net primary productivity in the complicated mountainous area: a case study of Yunnan, China. *IEEE J-STARS* 11 (12), 4637–4648.
- Guo, L.M., Sun, F.B., Liu, W.B., Zhang, Y.G., Wang, H., Cui, H.J., Wang, H.Q., Zhang, J., Du, B.X., 2019. Response of ecosystem water use efficiency to drought over China during 1982–2015: spatiotemporal variability and resilience. *Forests* 10 (7). <https://doi.org/10.3390/f10070598>.
- Heinsch, F.A., Reeves, M., Votava, P., Kang, S., Milesi, C., Zhao, M., Glassy, J., Jolly, W.M., Loehman, R., Bowker, C.F., 2003. *User's Guide GPP and NPP (MOD17A2/A3) Products NASA MODIS Land Algorithm* (Sioux Falls, South Dakota).
- Hinzman, L.D., Bettes, N.D., Bolton, W.R., Chapin, F.S., Dyurgerov, M.B., Fastie, C.L., Griffith, B., Hollister, R.D., Hope, A., Huntington, H.P., Jensen, A.M., Jia, G.J., Jorgenson, T., Kane, D.L., Klein, D.R., Kofinas, G., Lynch, A.H., Lloyd, A.H., McGuire, A.D., Nelson, F.E., Oechel, W.C., Osterkamp, T.E., Racine, C.H., Romanovsky, V.E., Stone, R.S., Stow, D.A., Sturm, M., Tweedie, C.E., Vourlitis, G.L., Walker, M.D., Walker, D.A., Webber, P.J., Welker, J.M., Winker, K., Yoshikawa, K., 2005. Evidence and implications of recent climate change in northern Alaska and other arctic regions. *Clim. Chang.* 72 (3), 251–298. <https://doi.org/10.1007/s10584-005-5352-2>.
- Huang, M.T., Piao, S.L., Sun, Y., Ciais, P., Cheng, L., Mao, J.F., Poulter, B., Shi, X.Y., Zeng, Z.Z., Wang, Y.P., 2015. Change in terrestrial ecosystem water-use efficiency over the last three decades. *Glob. Change Biol.* 21 (6), 2366–2378. <https://doi.org/10.1111/gcb.12873>.
- Huang, L., He, B., Han, L., Liu, J.J., Wang, H.Y., Chen, Z.Y., 2017. A global examination of the response of ecosystem water-use efficiency to drought based on MODIS data. *Sci. Total Environ.* 601, 1097–1107.
- Ise, T., Litton, C.M., Giardina, C.P., Ito, A., 2010. Comparison of modeling approaches for carbon partitioning: impact on estimates of global net primary production and equilibrium biomass of woody vegetation from MODIS GPP. *J. Geophys. Res.-Biogeo.* 115. <https://doi.org/10.1029/2010jg001326>.
- Jin, Z., Liang, W., Yang, Y.T., Zhang, W.B., Yan, J.W., Chen, X.J., Li, S., Mo, X.G., 2017. Separating vegetation greening and climate change controls on evapotranspiration trend over the loess plateau. *Sci. Rep.* 7. <https://doi.org/10.1038/s41598-017-08477-x>.
- Jung, M., Reichstein, M., Ciais, P., Seneviratne, S.I., Sheffield, J., Goulden, M.L., Bonan, G., Cescatti, A., Chen, J.Q., de Jeu, R., Dolman, A.J., Eugster, W., Gerten, D., Gianelle, D., Gobron, N., Heinke, J., Kimball, J., Law, B.E., Montagnani, L., Mu, Q.Z., Mueller, B., Oleson, K., Papale, D., Richardson, A.D., Rouspard, O., Running, S., Tomelleri, E., Viovy, N., Weber, U., Williams, C., Wood, E., Zaehle, S., Zhang, K., 2010. Recent decline in the global land evapotranspiration trend due to limited moisture supply. *Nature* 467 (7318), 951–954. <https://doi.org/10.1038/nature09396>.

- Knoblauch, C., Beer, C., Liebner, S., Grigoriev, M.N., Pfeiffer, E.-M., 2018. Methane production as key to the greenhouse gas budget of thawing permafrost. *Nat. Clim. Chang.* 8 (4), 309–312.
- Korner, C., Diemer, M., Schappi, B., Niklaus, P., Arnone, J., 1997. The responses of alpine grassland to four seasons of CO<sub>2</sub> enrichment: a synthesis. *Acta Oecol.* 18 (3), 165–175. [https://doi.org/10.1016/s1146-609x\(97\)80002-1](https://doi.org/10.1016/s1146-609x(97)80002-1).
- Koven, C.D., Lawrence, D.M., Riley, W.J., 2015. Permafrost carbon-climate feedback is sensitive to deep soil carbon decomposability but not deep soil nitrogen dynamics. *Proc. Natl. Acad. Sci. U. S. A.* 112 (12), 3752–3757. <https://doi.org/10.1073/pnas.1415123112>.
- Li, S.Y., Verburg, P.H., Lv, S.H., Wu, J.L., Li, X.B., 2012. Spatial analysis of the driving factors of grassland degradation under conditions of climate change and intensive use in Inner Mongolia, China. *Reg. Environ. Chang.* 12 (3), 461–474. <https://doi.org/10.1007/s10113-011-0264-3>.
- Liu, X., Feng, X., Fu, B., 2020. Changes in global terrestrial ecosystem water use efficiency are closely related to soil moisture. *Sci. Total Environ.* 698, 134165. <https://doi.org/10.1016/j.scitotenv.2019.134165>.
- Luo, Y., Su, B., Currie, W.S., Dukes, J.S., Finzi, A.C., Hartwig, U., Hungate, B., McMurtrie, R.E., Oren, R., Parton, W.J., Pataki, D.E., Shaw, M.R., Zak, D.R., Field, C.B., 2004. Progressive nitrogen limitation of ecosystem responses to rising atmospheric carbon dioxide. *BioScience* 54 (8), 731–739. [https://doi.org/10.1641/0006-3568\(2004\)054\[0731:pnloer\]2.0.co;2](https://doi.org/10.1641/0006-3568(2004)054[0731:pnloer]2.0.co;2).
- Lupascu, M., Wadham, J., Hornibrook, E., Pancost, R., 2012. Temperature sensitivity of methane production in the permafrost active layer at Stordalen, Sweden: a comparison with non-permafrost northern wetlands. *Arct. Antarct. Alp. Res.* 44 (4), 469–482.
- McGuire, A.D., Anderson, L.G., Christensen, T.R., Dallimore, S., Guo, L.D., Hayes, D.J., Heimann, M., Lorenson, T.D., Macdonald, R.W., Roulet, N., 2009. Sensitivity of the carbon cycle in the Arctic to climate change. *Ecol. Monogr.* 79 (4), 523–555. <https://doi.org/10.1890/08-2025.1>.
- Mu, Q., Zhao, M.S., Running, S.W., 2011. Improvements to a MODIS global terrestrial evapotranspiration algorithm. *Remote Sens. Environ.* 115 (8), 1781–1800. <https://doi.org/10.1016/j.rse.2011.02.019>.
- Mueller, B., Seneviratne, S.I., Jimenez, C., Corti, T., Hirschi, M., Balsamo, G., Ciais, P., Dirmeyer, P., Fisher, J.B., Guo, Z., Jung, M., Maignan, F., McCabe, M.F., Reichle, R., Reichstein, M., Rodell, M., Sheffield, J., Teuling, A.J., Wang, K., Wood, E.F., Zhang, Y., 2011. Evaluation of global observations-based evapotranspiration datasets and IPCC AR4 simulations. *Geophys. Res. Lett.* 38. <https://doi.org/10.1029/2010gl046230>.
- Oberbauer, S.F., Sionit, N., Hastings, S.J., Oechel, W.C., 1986. Effects of CO<sub>2</sub> enrichment and nutrition on growth, photosynthesis, and nutrient concentration of Alaskan tundra plant species. *Can. J. Bot.* 64 (12), 2993–2998. <https://doi.org/10.1139/b86-396>.
- O'Neill, B.C., Tebaldi, C., van Vuuren, D.P., Eyring, V., Friedlingstein, P., Hurtt, G., Knutti, R., Krieger, E., Lamarque, J.F., Lowe, J., Meehl, G.A., Moss, R., Riahi, K., Sanderson, B.M., 2016. The scenario model intercomparison project (ScenarioMIP) for CMIP6. *Geosci. Model Dev.* 9 (9), 3461–3482. <https://doi.org/10.5194/gmd-9-3461-2016>.
- Pan, S.F., Tian, H.Q., Dangal, S.R.S., Yang, Q.C., Yang, J., Lu, C.Q., Tao, B., Ren, W., Ouyang, Z.Y., 2015. Responses of global terrestrial evapotranspiration to climate change and increasing atmospheric CO<sub>2</sub> in the 21st century. *Earth's Future* 3 (1), 15–35. <https://doi.org/10.1002/2014ef000263>.
- Peterson, T.C., Golubev, V.S., Groisman, P.Y., 1995. Evaporation losing its strength. *Nature* 377 (6551), 687–688. <https://doi.org/10.1038/377687b0>.
- Propastin, P., Kappas, M., 2012. Assessing satellite-observed nighttime lights for monitoring socioeconomic parameters in the Republic of Kazakhstan. *Gisci Remote Sens* 49 (4), 538–557. <https://doi.org/10.2747/1548-1603.49.4.538>.
- Rawlins, A.M., McGuire, A.D., Kimball, J.S., Dass, P., Lawrence, D., Burke, E., Chen, X., Delire, C., Koven, C., MacDougall, A., Peng, S., Rinke, A., Saito, K., Zhang, W., Alkama, R., Bohn, T.J., Ciais, P., Decharme, B., Gouttevin, I., Hajima, T., Ji, D., Krinner, G., Lettenmaier, D.P., Miller, P., Moore, J.C., Smith, B., Sueyoshi, T., 2015. Assessment of model estimates of land-atmosphere CO<sub>2</sub> exchange across Northern Eurasia. *Biogeosciences* 12 (14), 4385–4405. <https://doi.org/10.5194/bg-12-4385-2015>.
- Reich, P.B., Hobbie, S.E., Lee, T., Ellsworth, D.S., West, J.B., Tilman, D., Knops, J.M.H., Naeem, S., Trost, J., 2006. Nitrogen limitation constrains sustainability of ecosystem response to CO<sub>2</sub>. *Nature* 440 (7086), 922–925. <https://doi.org/10.1038/nature04486>.
- Rigden, A.J., Salvucci, G.D., 2017. Stomatal response to humidity and CO<sub>2</sub> implicated in recent decline in US evaporation. *Glob. Change Biol.* 23 (3), 1140–1151. <https://doi.org/10.1111/gcb.13439>.
- Romanovsky, V.E., Drozdov, D.S., Oberman, N.G., Malkova, G.V., Kholodov, A.L., Marchenko, S.S., Moskalenko, N.G., Sergeev, D.O., Ukraintseva, N.G., Abramov, A.A., Gilichinsky, D.A., Vasiliev, A.A., 2010. Thermal state of permafrost in Russia. *Permafrost. Periglac. Process.* 21 (2), 136–155. <https://doi.org/10.1002/ppp.683>.
- Rowland, L., Hill, T.C., Stahl, C., Siebicke, L., Burban, B., Zaragoza-Castells, J., Ponton, S., Bonal, D., Meir, P., Williams, M., 2014. Evidence for strong seasonality in the carbon storage and carbon use efficiency of an Amazonian forest. *Glob. Change Biol.* 20 (3), 979–991. <https://doi.org/10.1111/gcb.12375>.
- Running, S.W., Nemani, R.R., Heinsch, F.A., Zhao, M.S., Reeves, M., Hashimoto, H., 2004. A continuous satellite-derived measure of global terrestrial primary production. *BioScience* 54 (6), 547–560. [https://doi.org/10.1641/0006-3568\(2004\)054\[0547:acsmoj\]2.0.co;2](https://doi.org/10.1641/0006-3568(2004)054[0547:acsmoj]2.0.co;2).
- Schuur, E.A.G., Bockheim, J., Canadell, J.G., Euskirchen, E., Field, C.B., Goryachkin, S.V., Hagemann, S., Kuhry, P., Lafleur, P.M., Lee, H., Mazhitova, G., Nelson, F.E., Rinke, A., Romanovsky, V.E., Shiklomanov, N., Tarnocai, C., Venevsky, S., Vogel, J.G., Zimov, S.A., 2008. Vulnerability of permafrost carbon to climate change: implications for the global carbon cycle. *BioScience* 58 (8), 701–714. <https://doi.org/10.1641/b580807>.
- Schuur, E.A.G., McGuire, A.D., Schädel, C., Grosse, G., Harden, J.W., Hayes, D.J., Hugelius, G., Koven, C.D., Kuhry, P., Lawrence, D.M., 2015. Climate change and the permafrost carbon feedback. *Nature* 520, 171–179. <https://doi.org/10.1038/nature14338>.
- Séférian, R., 2018. CNRM-CERFACS CNRM-ESM2-1 Model Output Prepared for CMIP6 CMIP. Version 20180816. Earth System Grid Federation <https://doi.org/10.22033/ESGF/CMIP6.1391>.
- Shiklomanov, N.I., 2005. From exploration to systematic investigation: development of geocryology in 19th- and early-20th-century Russia. *Phys. Geogr.* 26 (4), 249–263. <https://doi.org/10.2747/0272-3646.26.4.249>.
- Sjostrom, M., Zhao, M., Archibald, S., Arneeth, A., Cappelera, B., Falk, U., de Grandcourt, A., Hanan, N., Kergoat, L., Kutsch, W., Merbold, L., Mouglin, E., Nickless, A., Nouvellon, Y., Scholes, R.J., Veenendaal, E.M., Ardo, J., 2013. Evaluation of MODIS gross primary productivity for Africa using eddy covariance data. *Remote Sens. Environ.* 131, 275–286. <https://doi.org/10.1016/j.rse.2012.12.023>.
- Song, X., Tian, H., Xu, X., Hui, D., Chen, G., Sommers, G., Luke, M., Liu, M., 2013. Projecting terrestrial carbon sequestration of the southeastern United States in the 21st century. *Ecosphere* 4 (7). <https://doi.org/10.1890/ES12-00398.1>.
- Sun, Y., Piao, S.L., Huang, M.T., Ciais, P., Zeng, Z.Z., Cheng, L., Li, X.R., Zhang, X.P., Mao, J.F., Peng, S.S., Poulter, B., Shi, X.Y., Wang, X.H., Wang, Y.P., Zeng, H., 2016. Global patterns and climate drivers of water-use efficiency in terrestrial ecosystems deduced from satellite-based datasets and carbon cycle models. *Glob. Ecol. Biogeogr.* 25 (3), 311–323. <https://doi.org/10.1111/geb.12411>.
- Swart, N.C., Cole, J.N.S., Kharin, V.V., Lazare, M., Scinocca, J.F., Gillett, N.P., Anstey, J., Arora, V., Christian, J.R., Jiao, Y., Lee, W.G., Majaess, F., Saenko, O.A., Seiler, C., Seinen, C., Shao, A., Solheim, L., von Salzen, K., Yang, D., Winter, B., Sigmund, M., 2019. CCCma CanESM5 Model Output Prepared for CMIP6 ScenarioMIP. Version 20190501. Earth System Grid Federation <https://doi.org/10.22033/ESGF/CMIP6.1317>.
- Tang, X.G., Li, H.P., Desai, A.R., Nagy, Z., Luo, J.H., Kolb, T.E., Oliosio, A., Xu, X.B., Yao, L., Kutsch, W., Pilegaard, K., Kostner, B., Ammann, C., 2014. How is water-use efficiency of terrestrial ecosystems distributed and changing on Earth? *Sci. Rep.* 4. <https://doi.org/10.1038/srep07483>.
- Tian, H.Q., Chen, G.S., Liu, M.L., Zhang, C., Sun, G., Lu, C.Q., Xu, X.F., Ren, W., Pan, S.F., Chappellka, A., 2010. Model estimates of net primary productivity, evapotranspiration, and water use efficiency in the terrestrial ecosystems of the southern United States during 1895–2007. *For. Ecol. Manag.* 259 (7), 1311–1327. <https://doi.org/10.1016/j.foreco.2009.10.009>.
- Wang, Y., Yuan, F., Yuan, F., Gu, B., Hahn, M.S., Torn, M.S., Ricciuto, D.M., Kumar, J., He, L., Zona, D., Lipson, D.L., Wagner, R., Oechel, W.C., Wullschlegel, S.D., Thornton, P.E., Xu, X., 2019. Mechanistic modeling of microtopographic impact on CH<sub>4</sub> processes in an Alaskan tundra ecosystem using the CLM-microbe model. *J. Adv. Model Earth Sy.* 11, 4228–4304.
- Waring, R.H., Landsberg, J.J., Williams, M., 1998. Net primary production of forests: a constant fraction of gross primary production? *Tree Physiol.* 18 (2), 129–134.
- White, M.A., Running, S.W., Thornton, P.E., 1999. The impact of growing-season length variability on carbon assimilation and evapotranspiration over 88 years in the eastern US deciduous forest. *Int. J. Biometeorol.* 42 (3), 139–145. <https://doi.org/10.1007/s004840050097>.
- Wieder, W., Boehner, J., Bonan, G., Langseth, M., 2014. RegridDED Harmonized World Soil Database v1.2. from Oak Ridge National Laboratory Distributed Active Archive Center, Oak Ridge, Tennessee, USA Available on-line. <http://daac.ornl.gov>.
- Xia, L., Wang, F., Mu, X., Jin, K., Sun, W., Gao, P., Zhao, G., 2015. Water use efficiency of net primary production in global terrestrial ecosystems. *J. Earth Syst. Sci.* 124 (5), 921–931. <https://doi.org/10.1007/s12040-015-0587-4>.
- Xia, J.Y., McGuire, A.D., Lawrence, D., Burke, E., Chen, G.S., Chen, X.D., Delire, C., Koven, C., MacDougall, A., Peng, S.S., Rinke, A., Saito, K., Zhang, W.X., Alkama, R., Bohn, T.J., Ciais, P., Decharme, B., Gouttevin, I., Hajima, T., Hayes, D.J., Huang, K., Ji, D.Y., Krinner, G., Lettenmaier, D.P., Miller, P.A., Moore, J.C., Smith, B., Sueyoshi, T., Shi, Z., Yan, L.M., Liang, J.Y., Jiang, L.F., Zhang, Q., Luo, Y.Q., 2017. Terrestrial ecosystem model performance in simulating productivity and its vulnerability to climate change in the northern permafrost region. *J. Geophys. Res.-Biogeosci.* 122 (2), 430–446. <https://doi.org/10.1002/2016jg003384>.
- Xing, X.X., Xu, X.L., Zhang, X.Z., Zhou, C.P., Song, M.H., Shao, B., Ouyang, H., 2010. Simulating net primary production of grasslands in northeastern Asia using MODIS data from 2000 to 2005. *J. Geogr. Sci.* 20 (2), 193–204. <https://doi.org/10.1007/s11442-010-0193-y>.
- Xue, B.L., Guo, A.Otto, X., Tao, S., Li, L., 2015. Global patterns, trends, and drivers of water use efficiency from 2000 to 2013. *Ecosphere* 6 (10), 174.
- Xu, X., Elias, D.A., Graham, D.E., Phelps, T.J., Carroll, S.L., Wullschlegel, S.D., Thornton, P.E., 2015. A microbial functional group-based module for simulating methane production and consumption: application to an incubated permafrost soil. *J. Geophys. Res.-Biogeosci.* 120 (7), 1315–1333.
- Xu, X., Yuan, F., Hanson, P.J., Wullschlegel, S.D., Thornton, P.E., Riley, W.J., Song, X., Graham, D.E., Song, C., Tian, H., 2016. Reviews and syntheses: four decades of modeling methane cycling in terrestrial ecosystems. *Biogeosciences* 13 (12), 3735–3755. <https://doi.org/10.5194/bg-13-3735-2016>.
- Yan, H., Yu, Q., Zhu, Z.C., Myneni, R.B., Yan, H.M., Wang, S.Q., Shugart, H.H., 2013. Diagnostic analysis of interannual variation of global land evapotranspiration over 1982–2011: assessing the impact of ENSO. *J. Geophys. Res.-Atmos.* 118 (16), 8969–8983. <https://doi.org/10.1002/jgrd.50693>.
- Yang, Z.S., Zhang, Q., Hao, X.C., Yue, P., 2019. Changes in evapotranspiration over global semiarid regions 1984–2013. *J. Geophys. Res.-Atmos.* 124 (6), 2946–2963. <https://doi.org/10.1029/2018jd029533>.
- Zeng, Z.Z., Piao, S.L., Lin, X., Yin, G.D., Peng, S.S., Ciais, P., Myneni, R.B., 2012. Global evapotranspiration over the past three decades: estimation based on the water balance equation combined with empirical models. *Environ. Res. Lett.* 7 (1). <https://doi.org/10.1088/1748-9326/7/1/014026>.
- Zhang, F., Ju, W., Shen, S., Wang, S., Yu, G., Han, S., 2014a. How recent climate change influences water use efficiency in East Asia. *Theor. Appl. Clim.* 116 (1), 359–370. <https://doi.org/10.1007/s00704-013-0949-2>.



- Zhang, Y.J., Yu, G.R., Yang, J., Wimberly, M.C., Zhang, X.Z., Tao, J., Jiang, Y.B., Zhu, J.T., 2014b. Climate-driven global changes in carbon use efficiency. *Glob. Ecol. Biogeogr.* 23 (2), 144–155. <https://doi.org/10.1111/geb.12086>.
- Zhang, K., Kimball, J., Nemani, R.R., Running, S.W., Hong, Y., Gourley, J.J., Yu, Z.B., 2015. Vegetation greening and climate change promote multidecadal rises of global land evapotranspiration. *Sci. Rep.* 5. <https://doi.org/10.1038/srep15956>.
- Zhang, H., McDowell, N.G., Adams, H.D., Wang, A., Wu, J., Jin, C., Tian, J., Zhu, K., Li, W., Zhang, Y., Yuan, F., Guan, D., 2020. Divergences in hydraulic conductance and anatomical traits of stems and leaves in three temperate tree species coping with drought, N addition and their interactions. *Tree Physiol.* 40 (2), 230–244. <https://doi.org/10.1093/treephys/tpz135>.
- Zhang, Y., Peña-Arancibia, J.L., McVicar, T.R., Chiew, F.H.S., Vaze, J., Liu, C., Lu, X., Zheng, H., Wang, Y., Liu, Y.Y., Miralles, D.G., Pan, M., 2016. Multi-decadal trends in global terrestrial evapotranspiration and its components. *Sci. Rep.* 6 (1), 19124. <https://doi.org/10.1038/srep19124>.
- Zhao, M., Heinsch, F.A., Nemani, R.R., Running, S.W., 2005. Improvements of the MODIS terrestrial gross and net primary production global data set. *Remote Sens. Environ.* 95 (2), 164–176. <https://doi.org/10.1016/j.rse.2004.12.011>.
- Zhao, M., Running, S.W., Nemani, R.R., 2006. Sensitivity of Moderate Resolution Imaging Spectroradiometer (MODIS) terrestrial primary production to the accuracy of meteorological reanalyses. *J. Geophys. Res.-Biogeophys.* 111 (G1). <https://doi.org/10.1029/2004jg000004>.
- Zhu, Z.C., Piao, S.L., Myneni, R.B., Huang, M.T., Zeng, Z.Z., Canadell, J.G., Ciais, P., Sitch, S., Friedlingstein, P., Arneth, A., Cao, C.X., Cheng, L., Kato, E., Koven, C., Li, Y., Lian, X., Liu, Y.W., Liu, R.G., Mao, J.F., Pan, Y.Z., Peng, S.S., Penuelas, J., Poulter, B., Pugh, T.A.M., Stocker, B.D., Viovy, N., Wang, X.H., Wang, Y.P., Xiao, Z.Q., Yang, H., Zaehle, S., Zeng, N., 2016. Greening of the Earth and its drivers. *Nat. Clim. Chang.* 6 (8), 791–795. <https://doi.org/10.1038/nclimate3004>.